

# Energy spectra of light charged particles emitted following muon nuclear capture on $^{nat}\text{Si}$

Shoichiro Kawase (川瀬頌一郎),<sup>1, 2, 3,\*</sup> Kentaro Kitafuji (北藤健太郎),<sup>1</sup> Teppei Kawata (川田哲平),<sup>1</sup> Yukinobu Watanabe (渡辺幸信),<sup>1, 2</sup> Megumi Niikura (新倉潤),<sup>3</sup> Teiichiro Matsuzaki (松崎禎市郎),<sup>3</sup> Katsuhiko Ishida (石田勝彦),<sup>4</sup> Rurie Mizuno (水野るり恵),<sup>5</sup> Dai Tomono (友野大),<sup>6</sup> Adrian D. Hillier,<sup>7</sup> Futoshi Minato (湊太志),<sup>8</sup> and Shin-ichiro Abe (安部晋一郎)<sup>9</sup>

<sup>1</sup>Department of Advanced Energy Science and Engineering, Kyushu University, Kasuga, Fukuoka 816-8580, Japan

<sup>2</sup>Quantum and Spacetime Research Institute, Kyushu University, Fukuoka, Fukuoka 819-0395, Japan

<sup>3</sup>RIKEN Nishina Center, Wako, Saitama 351-0198, Japan

<sup>4</sup>High Energy Accelerator Research Organization (KEK), Tsukuba, Ibaraki 305-0801, Japan

<sup>5</sup>Department of Physics, Graduate School of Science, The University of Tokyo, Bunkyo, Tokyo 113-0033, Japan.

<sup>6</sup>Research Center for Nuclear Physics, Osaka University, Mihogaoka 10-1, Osaka 567-0047, Japan

<sup>7</sup>Science and Technology Facilities Council Rutherford Appleton Laboratory, Didcot, Oxfordshire OX11 0QX, United Kingdom

<sup>8</sup>Department of Physics, Kyushu University, Fukuoka, Fukuoka 819-0395, Japan

<sup>9</sup>Japan Atomic Energy Agency (JAEA), Tokai, Ibaraki 319-1195, Japan

(Dated: January 15, 2026)

**Background:** Charged-particle emission following muon nuclear capture ( $\mu\text{NC}$ ) provides unique information on the de-excitation dynamics of highly excited nuclei, particularly on the interplay between preequilibrium and evaporation processes. While proton emission has been relatively well studied, experimental data on composite charged particles remain limited, especially in the low-energy region for  $\alpha$  particles.

**Purpose:** This work aims to measure comprehensive energy spectra of charged particles emitted following  $\mu\text{NC}$  on silicon and to provide experimental constraints on existing theoretical models describing charged-particle emission.

**Method:** An experiment was performed at the RIKEN-RAL Muon Facility. Charged particles were identified using a combination of  $\Delta E-E$  telescopes and digital pulse-shape analysis with nTD-Si detectors. The initial energy spectra were reconstructed through an unfolding procedure and compared with calculations based on the microscopic and evaporation model (MEM), as well as the PHITS code incorporating the surface coalescence model and the meson-exchange-current extension.

**Results:** Energy spectra of protons, deuterons, tritons, and  $\alpha$  particles were successfully extracted over a broad energy range. In particular, the low-energy  $\alpha$ -particle spectrum was measured for the first time. The proton spectra are reproduced reasonably well by both MEM and PHITS. For  $\alpha$  particles, the low-energy component dominated by evaporation is described by both models, whereas discrepancies remain at higher energies. For deuterons and tritons, MEM reproduces the spectral shapes well, while PHITS significantly underestimates the yields, especially in the high-energy region.

**Conclusion:** The present results demonstrate clear particle-species-dependent differences in charged-particle emission following  $\mu\text{NC}$ . The comprehensive energy spectra obtained in this work provide valuable constraints on theoretical descriptions of preequilibrium and evaporation processes and highlight the need for improved modeling of composite-particle emission.

## I. INTRODUCTION

When a negative muon stops in matter, it can be captured by an atomic nucleus with a certain probability, leading to muon nuclear capture ( $\mu\text{NC}$ ) [1]. This process excites the nucleus to energies ranging from several to several tens of MeV, typically well above the particle emission threshold. The highly excited nucleus subsequently de-excites through the emission of various particles, including neutrons, protons, deuterons, and alpha particles, and finally, gamma rays.

Particle emission following  $\mu\text{NC}$  proceeds via multiple reaction mechanisms that occur on different time

scales — namely, direct reactions, preequilibrium processes, and statistical evaporation. Each mechanism contributes differently to the energy spectra of the emitted particles: direct reactions contribute to the high-energy component, typically above a couple of tens of MeV, with an exponential fall-off, the evaporation process dominates the low-energy region below a few MeV, and the preequilibrium process contributes to the intermediate energy range [2].

In contrast to neutron emission, which predominantly reflects the overall excitation energy and level density of the compound nucleus, charged-particle emission provides complementary information on the particle-emission mechanism. While neutron emission is largely governed by statistical evaporation, charged-particle emission is strongly affected by the Coulomb barrier and by the manner in which the particles are formed

\* shkawase@kyudai.jp

and emitted. In particular, the emission of composite charged particles, such as deuterons, tritons, and  $\alpha$  particles, raises fundamental questions about their formation mechanism. These particles may be emitted as preformed clusters reflecting intrinsic correlations inside the nucleus, or they may be formed dynamically through the coalescence of independently emitted nucleons during the emission process. Disentangling these scenarios requires detailed information on charged-particle energy spectra, making charged particle emission a uniquely sensitive probe of correlation effects in nuclear decay. In the case of nuclear muon capture, where the nucleus is driven to high excitation energy with relatively low angular momentum, such questions regarding the formation mechanism of composite charged particles can be addressed under well-defined experimental conditions, as muon nuclear capture does not involve incident nucleon or heavy-ion beams and thus avoids backgrounds originating from beam-induced nuclear reactions.

However, indirect approaches based on the production probabilities of residual nuclei, as measured by activation measurements [3–6] and prompt gamma-ray detection [7–14], cannot distinguish between different particle emission processes leading to the same reaction channels; for example,  $1p1n$  emission and deuteron emission cannot be discriminated. Moreover, such approaches do not resolve how the available decay strength is distributed among the various charged-particle channels. Similarly, discussions based solely on integrated branching ratios, while informative, do not provide access to the underlying emission dynamics encoded in the energy spectra. A direct experimental study of charged-particle emission is therefore essential to fully exploit the well-defined reaction condition provided by  $\mu$ NC, to disentangle the underlying emission mechanisms, and to access the detailed information encoded in the energy spectra.

In the present work, charged-particle emission following  $\mu$ NC on silicon was investigated. The motivation for focusing on silicon in the present study is threefold. First, charged-particle emission after  $\mu$ NC is suppressed by the Coulomb barrier and becomes progressively less probable with increasing atomic number [3–5, 15, 16]. As a result, light to medium-mass nuclei, up to around the Ca region, provide favorable conditions under which charged-particle emission can be observed with sufficient yield to enable systematic discussion of the emission mechanisms. Second, although silicon has been investigated in several previous experiments [17–20], the available experimental data remain limited. In particular, existing datasets are fragmented in energy coverage and lack information in the low-energy part of the  $\alpha$  spectrum. Third,  $\alpha$  particles play a central role in the statistical evaporation process. Since  $\alpha$ -particle emission occurs universally above a certain excitation-energy threshold, the shape of the  $\alpha$ -particle energy spectrum provides essential constraints on the evaporation component and on the formation mechanisms of composite charged particles. In this respect, silicon is a self-conjugate nucleus ( $N = Z$ ),

for which  $\alpha$ -cluster correlations are expected to be relatively favored compared to non-self-conjugate systems. Although the present work does not aim to probe nuclear structure directly, this property makes Si suitable for investigating  $\alpha$  and other composite charged-particle emissions following  $\mu$ NC.

Beyond its relevance to nuclear reaction dynamics, accurate knowledge of low-energy charged particle spectra, particularly for protons and  $\alpha$  particles, is also important from an applied perspective. In semiconductor devices, cosmic-ray muons have been identified as a potential source of radiation-induced failures, and low-energy charged particles produced via  $\mu$ NC can contribute to soft error rates [21–23].

This paper is organized as follows. Section II describes the experimental setup, including the muon beam conditions, target configuration, and the detector system optimized for low-energy charged particle measurements. Section III outlines the data reduction procedures, including event selection, energy calibration, and particle identification methods. The experimental results are presented in Section IV, with a focus on the energy spectra of emitted charged particles. In Section V, the results are discussed in the context of nuclear reaction mechanisms and compared with existing data and theoretical model calculations. Finally, Section VI summarizes the conclusions of this work and provides perspectives for future studies.

## II. EXPERIMENT

The experiment was performed at the RIKEN-RAL Muon Facility [24, 25] located at the Rutherford Appleton Laboratory (RAL), the UK. At this facility, 800 MeV protons accelerated by the ISIS synchrotron were directed onto a 10-mm-thick graphite target installed at the Target Station 1 (TS1) to produce pions. The generated pions were extracted via quadrupole magnets, and then the beam is bent into a solenoid where the pions decay in flight to muons. This muon beam was transported to Port 4 by using magnets.

The ISIS synchrotron operates at a repetition rate of 50 Hz with a double-bunch structure. Of these pulses, four out of every five were delivered to the TS1 target, resulting in an effective repetition rate of 40 pulses per second at TS1.

The reaction target and detectors were installed inside an aluminum vacuum chamber placed at Port 4 of the RIKEN-RAL facility. The vacuum chamber was not directly connected to the beam duct; instead, the muon beam passed through two polyimide vacuum windows of 50 and 75  $\mu$ m thickness, separated by a 5 cm air gap, before entering the chamber. A schematic diagram and photograph of the experimental setup around the target region are shown in Fig. 1.

To restrict the beam size, a tubular collimator with an inner diameter of 40 mm was installed in the vacuum

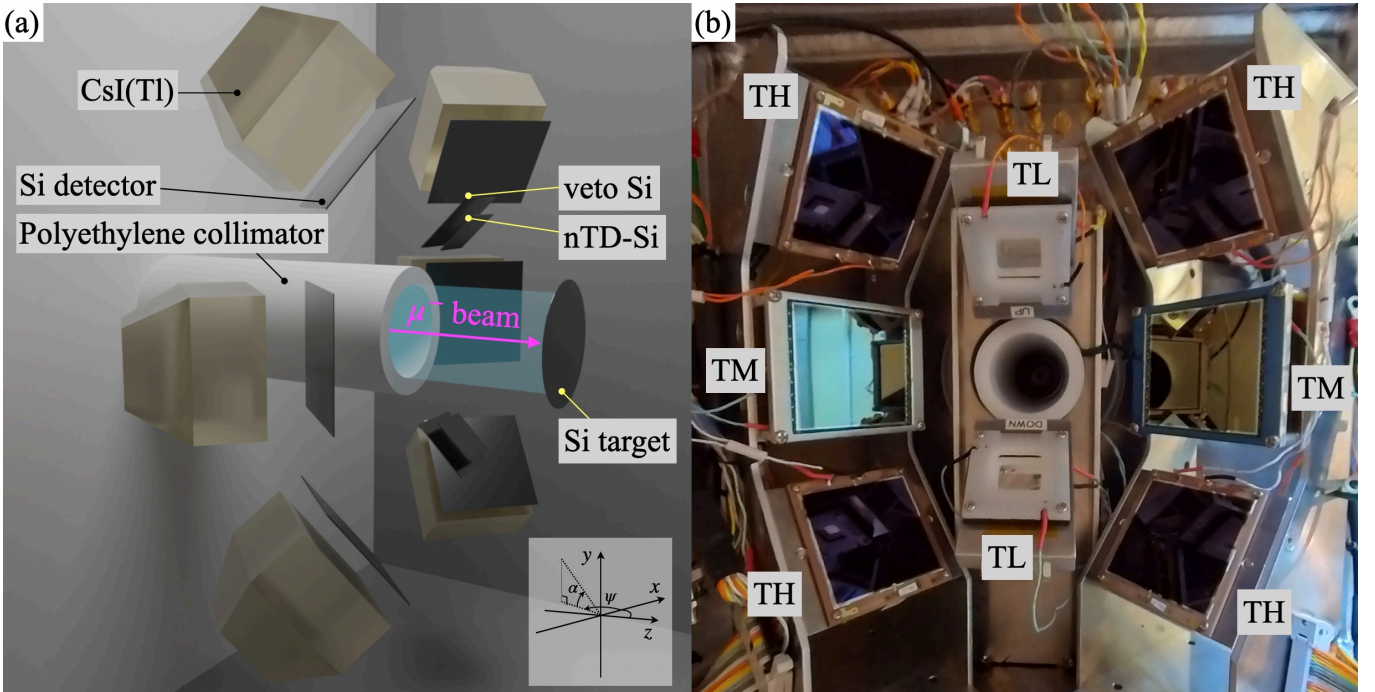


FIG. 1. Experimental setup around the Si target. (a) Schematic view of the detector arrangement around the target. Only the sensitive region of each detector is illustrated for simplicity. (b) Photograph of the actual setup installed in the vacuum chamber.

chamber upstream of the target. Both the target ladder and the collimator were made of polyethylene to suppress background events originating from  $\mu$ NC occurring outside the target region. This material was chosen because low- $Z$  substances, such as polyethylene, exhibit a significantly lower probability for  $\mu$ NC ( $\sim 6\%$  for C) compared to Si ( $\sim 66\%$ ).

Two silicon wafers, both with a diameter of 50.8 mm but different thicknesses, were used as reaction targets. A thin target with a thickness of 27  $\mu\text{m}$  was employed to measure low-energy spectra, while a thick target of 200  $\mu\text{m}$  was used to improve statistics in the high-energy region, where the particle emission probability is relatively low. To maximize the number of muons stopping within each target, the nominal muon beam momenta were set to 18.0 MeV/c for the thin target and 21.5 MeV/c for the thick target.

To detect charged particles over a wide range of kinetic energies, measure their deposited energies, and identify particle species, two types of detector telescopes were employed, as summarized in Table I. Hereafter, the individual detector telescopes are referred to as TL, TM, and TH, according to their positions around the target.

The TM and TH telescopes employed conventional  $\Delta E$ - $E$  configurations, each consisting of a silicon (Si) detector and a CsI(Tl) scintillator, and were used for energy measurement and particle identification in the high-energy region. Two Si photodiodes with different thicknesses were employed as the  $\Delta E$  detector: one was a Hamamatsu Photonics 50x50x325T-PD 0899 with a

thickness of 325  $\mu\text{m}$ , and the other was a Hamamatsu Photonics S14536-500 with a thickness of 500  $\mu\text{m}$ . Using detectors with different thicknesses allowed complementary coverage in energy and helped eliminate insensitive gaps in the energy spectra. The scintillation light from the CsI(Tl) was read out using a PIN photodiode (Hamamatsu Photonics S3584-08).

The TL telescope combined a neutron-transmutation-doped (nTD) Si detector (Micron Semiconductor MSX04-500 Type NTD) with an additional Si detector (Hamamatsu Photonics S14537-500) used as a veto for penetrating particles. Both Si detectors had a thickness of 500  $\mu\text{m}$ . This system enabled energy-deposit measurement and the identification of low-energy charged particles through a digital pulse shape analysis (DPSA) method [26].

To optimize particle identification capability, a low bias voltage is preferred for the nTD Si detectors, as long as sufficient charge collection efficiency and energy resolution are maintained. In this experiment, a bias voltage of 260 V was applied to nTD Si detectors as in Ref. [26]. In addition, a 3-mm-thick polyethylene collimator with an 18 mm  $\times$  18 mm square aperture was placed in front of each nTD-Si detector. This collimator was employed primarily to limit the effective sensitive area of the nTD-Si detector and to prevent the deterioration of particle identification performance near its edges [26].

The geometric configuration of the detector telescopes is summarized in Table II. The detector positions are described using two angular coordinates,  $\psi$  and  $\alpha$ . A right-

TABLE I. Specifications of detectors used in each telescope and their applied bias voltages.

Telescope	Detector	Size	Thickness	Bias	Voltage
TL	nTD-Si detector MSX04-500 (Micron)	20 mm $\times$ 20 mm	500 $\mu\text{m}$	260	V
TL	Si detector S14537-500 (Hamamatsu)	28 mm $\times$ 28 mm	500 $\mu\text{m}$	100	V
TM	Si detector 50x50x325T-PD 0899 (Hamamatsu)	50 mm $\times$ 50 mm	325 $\mu\text{m}$	70	V
TH	Si detector S14536-500 (Hamamatsu)	48 mm square	500 $\mu\text{m}$	150	V
TH, TM	CsI(Tl) scintillator (truncated pyramid)	50 mm square (base)	25 mm	100	V
	CsI(Tl) scintillator (top of truncated pyramid)	28 mm square (top)	22 mm		

TABLE II. Number of telescopes and their geometric configurations. The detector positions are described using two angular coordinates:  $\psi$  and  $\alpha$ . Here,  $\psi$  is the azimuthal angle measured anticlockwise in the  $zx$ -plane from the  $z$ -axis, and  $\alpha$  is the elevation angle from the  $zx$ -plane. The distance corresponds to that between the center of the target and the center of the surface of each detector.

Telescope Number	$(\psi, \alpha)$	Distance (mm)	$\Delta\Omega$ (msr)
TH	4 $\pm 130^\circ, \pm 40^\circ$	113.2	144.8
TM	2 $\pm 130^\circ, 0^\circ$	100.7	143.6
TL	2 $180^\circ, \pm 45^\circ$	64.8	75.6

handed Cartesian coordinate system is adopted, with the  $z$  axis defined along the muon beam direction and the  $y$  axis along the vertical direction. Here,  $\psi$  is defined as the angle in the  $zx$ -plane measured from the  $z$  axis, and  $\alpha$  is the elevation angle measured from the  $zx$ -plane. These angles are used solely to specify the detector geometry in this experiment and differ from the conventional spherical coordinate definitions. To reduce background events caused by muons scattered in the target, all detector telescopes were placed upstream of the target.

To measure the number of incoming muons and those penetrating the target per pulse, a plastic scintillator with dimensions of 50 mm  $\times$  70 mm and a thickness of 0.5 mm was placed 1 cm downstream of the target. The scintillation light was read out from one side using a photomultiplier tube (Hamamatsu Photonics H11934-100). This scintillator was used only during beam tuning phase and was removed during the physics measurement runs, as it would otherwise contribute to background events.

Analog signals from Si detectors and CsI(Tl) scintillators were amplified using charge-sensitive preamplifiers (Fuji-diamond International Co., Ltd. 0380-16). The amplified signals were then digitized with 14-bit resolution at a sampling rate of 500 MHz using waveform digitizers (CAEN SpA V1730SB), and transferred to a PC. The waveform record length was set to 20  $\mu\text{s}$ , which is sufficiently longer than the lifetime of the negative muon.

Due to hardware limitations of the V1730SB [27], specifically, that waveform readout is performed per channel pair and the associated buffer capacity is insufficient for recording 20  $\mu\text{s}$  waveforms from all 16 channels simultaneously. To circumvent this limitation, two digitizer modules were employed, and detector signals were connected to every other input channel, *i.e.*, only even-

numbered channels were used. This configuration ensured that each channel pair processed at most a single detector signal, allowing full-length waveform acquisition for all channels without loss. Waveform data were recorded using the CAEN Multi-Parameter Software (CoMPASS) and transferred to a PC for offline analysis.

To synchronize data acquisition with the pulse structure of the negative muon beam, a 50-Hz timing signal synchronized with the primary proton beam was fed into the V1730SB digitizer as an external trigger. Upon each trigger, waveforms from all detector channels were simultaneously recorded. The timing of the external trigger was adjusted so that the recorded waveform included at least 1  $\mu\text{s}$  of data prior to the muons' arrival, ensuring adequate coverage of the baseline and signal rise. Waveform acquisition was thus performed at fixed beam timing, regardless of whether a charged particle was detected in the telescopes or not, and even during beam cycles in which no protons were delivered to TS1. Since the digitizer continuously recorded waveforms upon each trigger without requiring per-event decisions, the data acquisition was effectively free from dead time.

### III. ANALYSIS

This section describes the data analysis procedures used to extract the energy spectra of particles emitted following  $\mu\text{NC}$ . The primary objective of the analysis is to obtain the initial energy spectrum of charged particles emitted following  $\mu\text{NC}$ , denoted as  $dN_{\text{init}}/dE$ .

Experimentally, however, what is directly measured is a distorted spectrum,  $dN_{\text{meas}}/dE$ , due to energy loss and straggling in the target material. The measured spectrum was calculated from the experimental yields using the following formula:

$$\frac{dN_{\text{meas}}}{dE}(E) = \frac{4\pi}{\Delta\Omega} \cdot \frac{Y(E)}{N_{\text{capture}} \cdot \Delta E}, \quad (1)$$

where  $Y(E)$  is the number of counts in each energy bin of width  $\Delta E$ ,  $\Delta\Omega$  is the solid angle covered by the detector, and  $N_{\text{capture}}$  is the total number of muon capture events. The factor  $4\pi/\Delta\Omega$  accounts for the extrapolation of the measured yield to the full solid angle, assuming isotropic emission.

To correct for the distortion caused by energy loss in the target, the initial spectrum  $dN_{\text{init}}/dE$  was obtained

TABLE III. Experimental parameters used to determine  $N_{\text{stop}}$ .

Target thickness ( $\mu\text{m}$ )	beam momentum ( $\text{MeV}/c$ )	$\bar{I}_{\text{out}}$ (nA)	$\bar{I}_{\text{in}}$ (nA)	$Q_{\text{meas}}$ ( $\text{mC}$ )
200	21.5	137.4	137.0	14.48
27	18.0	137.8	137.6	16.43

by applying an unfolding analysis to the measured spectrum  $dN_{\text{meas}}/dE$ .

In the following, we describe the procedures for determining  $N_{\text{capture}}$ , identifying charged particles, reconstructing their energies, performing unfolding analysis, and evaluating systematic uncertainties.

### A. Number of stopped muons

To determine the charged-particle energy spectrum per muon capture, the observed spectra were normalized to the number of muon captures in the silicon target,  $N_{\text{capture}}$ . The number of muon captures was obtained by multiplying the number of stopped muons,  $N_{\text{stop}}$ , by the muon capture probability in natural silicon, 65.9(1)%, which was calculated from the muon capture rate reported in Ref. [28]. The number of stopped muons was inferred using a plastic scintillator placed just downstream of the target.

The number of stopped muons  $N_{\text{stop}}$  was calculated using the following formula:

$$N_{\text{stop}} = f \cdot \left( \frac{n_{\text{out}}}{\bar{I}_{\text{out}}} - \frac{n_{\text{in}}}{\bar{I}_{\text{in}}} \right) Q_{\text{meas}} \quad (2)$$

where  $f$  is the frequency of proton beam pulses, i.e. 40 pulses per second, and  $n$  denotes the number of muons stopped in the plastic scintillator per pulse. The subscripts “in” and “out” correspond to configurations with and without the Si target, respectively.  $\bar{I}$  is the average proton beam current incident on the pion production target, measured during each configuration.  $Q_{\text{meas}}$  is the total proton beam charge accumulated during the spectrum measurement. The values of  $\bar{I}$  and  $Q_{\text{meas}}$  used in this work are summarized in Table III.

The plastic scintillator used in this study had a thickness of 0.5 mm, which is sufficient to stop negative muons with momenta of 21.5  $\text{MeV}/c$  and 18.0  $\text{MeV}/c$ . The number of stopped muons per pulse,  $n$ , was therefore estimated by performing peak searches on the digitized waveform signals from the plastic scintillator placed downstream of the target.

Figure 2 shows a typical waveform of the plastic scintillator from the PMT. In the present analysis, a “peak” is defined as a local maximum in the digitized waveform exceeding a predefined threshold. The time bin at which the waveform reaches this local maximum is referred to as the *peak timing*.

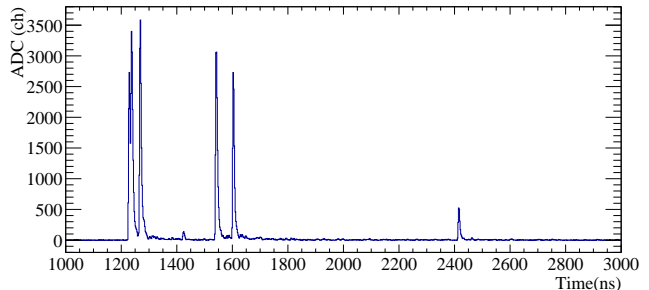


FIG. 2. Digitized waveform of the plastic scintillator from the photomultiplier tube obtained for the 21.5  $\text{MeV}/c$  muon beam run without the target. In this waveform, three muons reach the scintillator in the first beam bunch and two muons in the second beam bunch. Peaks observed around 1,425 ns and 2,415 ns are attributed to electrons originating from muon decay.

To quantify the signal associated with each peak, a *peak integral* was calculated by summing the waveform amplitudes over a fixed time window from  $-2$  to  $+3$  bins relative to the peak timing. This integration window was chosen to capture the full pulse shape while minimizing the contribution from electronic noise and neighboring pulses.

These waveform peaks include not only negative muons but also electrons. The electron component has two origins: electrons produced at the pion production target by the primary proton beam and subsequently transported as contaminants in the muon beam, and decay electrons from muons. Electrons originating from the pion production target are strongly suppressed by a DC separator installed in the beamline and therefore provide only a minor contribution. However, decay electrons from muons that pass through the DC separator may still reach the scintillator and generate spurious peaks.

The contribution from these electrons was evaluated using both the peak timing and waveform integral information. In the following subsections, we describe the procedure used to estimate the number of stopped muons  $n$  for each beam momentum and target thickness.

#### 1. $n_{\text{out}}$ for the 21.5 $\text{MeV}/c$ run

To determine the number of stopped muons per pulse  $n_{\text{out}}$ , we analyzed the digitized waveform signals from the plastic scintillator placed downstream of the target, using peak search techniques.

Figure 3 (a) shows a two-dimensional histogram of the peak timing and integrated peak value obtained from the plastic scintillator waveform with the target removed. Two distinct loci with integrated values around 10,000 are observed at timing windows of 1,160–1,340 ns and 1,500–1,680 ns, corresponding to the arrival of negative muons in the first and second beam bunches, respectively. The double structure reflects the inherent double-

bunched time structure of the primary proton beam.

In contrast, a broad distribution of peaks with low integrated values appears at later times, indicating decay electrons. As electrons produced during muon production are largely suppressed by the DC separator in the beamline, these later peaks are attributed primarily to decay electrons from muons that passed through the separator and subsequently stopped in the scintillator.

Figure 3 (b) shows the projection of the two-dimensional histogram (a) onto the timing axis, restricted to events with integrated values above 4,000 ch. This cut reduces the contribution from decay electrons and isolates the timing structure of the muon signals.

The resulting distribution was fitted using a composite function consisting of Gaussian peaks for the muon and electron signals and a decay-convolved Gaussian component representing the contribution from decay electrons. The explicit form of the fitting function is provided in Appendix A.

The number of stopped muons in the scintillator was evaluated by integrating the two Gaussian components corresponding to the muon pulses. Before applying the pileup correction, the estimated number of stopped muons per pulse pair was  $3.531 \pm 0.017$ .

This indicates that events in which multiple muons arrive within a single pulse window are present, and that the resulting pileup effects are not negligible. The pileup probability was estimated to be 15.6% using a Monte Carlo simulation, assuming that peaks separated by more than 6 ns can be resolved. A correction corresponding to this pileup probability was applied, resulting in  $n_{\text{out}} = 4.080 \pm 0.020$ .

The statistical uncertainty was evaluated using the covariance matrix obtained from the fit. The decay time constant extracted from the exponential component was found to be consistent with the known mean lifetime of negative muons in carbon, supporting the interpretation of the tail as originating from decay electrons in the scintillator.

## 2. $n_{\text{in}}$ for the 21.5 MeV/c run with a 200- $\mu\text{m}$ target

The determination of  $n_{\text{in}}$  for the 21.5 MeV/c run with the 200- $\mu\text{m}$  target was performed in the same manner as in the target-removed case, using the timing distribution of peaks identified in the plastic scintillator waveform. However, with the 200- $\mu\text{m}$  target in place, the energy deposition by muons in the scintillator is reduced due to energy loss in the target material. As a result, muon and electron signals cannot be clearly distinguished based on the peak integral alone. In the present analysis, this limitation does not affect the determination of the stopped-muon yield, since the timing distribution was analyzed by fitting both muon and electron components above a sufficiently low threshold.

Figure 4 (a) shows a two-dimensional histogram of peak timing versus integrated peak value. Unlike the

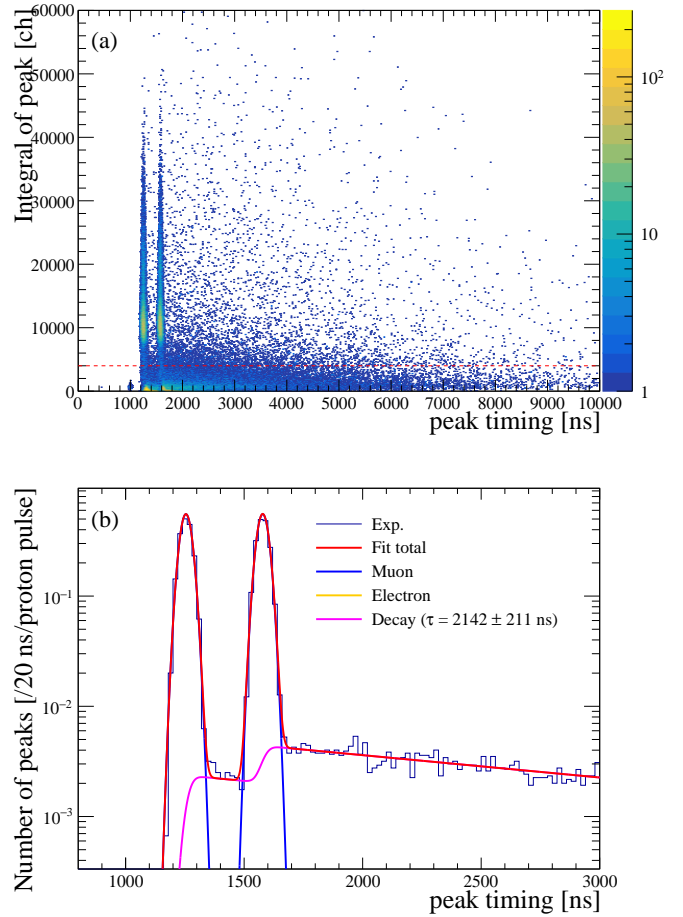


FIG. 3. Beam timing structure in the 21.5 MeV/c beam run with the target removed. (a) Two-dimensional histogram of peak timing versus integrated waveform value obtained from the plastic scintillator. Two distinct loci corresponding to the first and second muon pulses are clearly visible. The applied threshold on the integrated value is indicated by the red dashed line. (b) Timing distribution of peaks with integrated values above 4,000 ch, projected from the top panel. The data were fitted with a composite function including Gaussian components for muon and electron peaks and an exponential background for decay electrons. The decay time constant extracted from the fit is also shown in the figure.

target-removed case, the muon-related structures are less distinct and significantly overlap with decay-electron signals.

To extract the muon signal, a lower threshold of 300 ch was applied to the integrated value, and the resulting peaks were projected onto the timing axis. The timing distribution is shown in Fig. 4 (b). The fit was performed using the same functional form as in Appendix A.

As in the target-removed case, the number of stopped muons was evaluated by integrating the two Gaussian components corresponding to the muon pulses. The estimated number of stopped muons per pulse pair is  $n_{\text{in}} = 0.182 \pm 0.006$ .

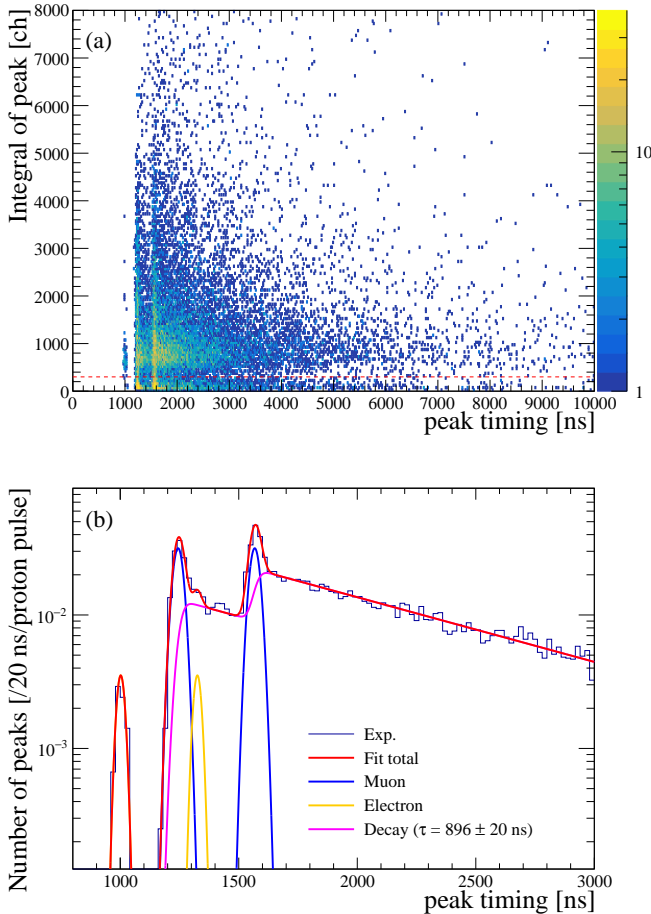


FIG. 4. Beam timing structure for the 21.5 MeV/c run with the target in place. (a) Two-dimensional histogram of peak timing versus integrated waveform value. Due to energy loss in the target, the muon loci are less distinct than in the target-removed case. The applied threshold on the integrated value is indicated by the red dashed line. (b) Timing distribution of peaks after applying an integrated-value threshold of 300 ch. The distribution is fitted using the model described in Appendix A.

The statistical uncertainty was derived from the covariance matrix of the fit. The decay constant obtained from the exponential component is  $\tau = (896 \pm 20)$  ns. This value lies between the lifetimes of negative muons in silicon ( $\sim 767$  ns) and in carbon ( $\sim 2,026$  ns) [28], consistent with that the decay component includes a mixture of muons stopped in the target and the plastic scintillator.

Because the average number of muons per bunch is significantly below one in this case, the probability of pileup is negligible.

### 3. $n_{\text{out}}$ for the 18.0 MeV/c run

The determination of  $n_{\text{out}}$  for the 18.0 MeV/c run was performed in the same manner as for the 21.5 MeV/c run, using the timing distribution of peaks identified in the plastic scintillator waveform without the target.

Compared to the 21.5 MeV/c target-out run, the separation between muon and decay-electron components is less distinct due to the lower beam momentum. At 18.0 MeV/c, muons are more strongly slowed before reaching the scintillator, resulting in reduced energy deposition and greater overlap with decay-electron signals. This situation is similar to that observed in the target-in case at 21.5 MeV/c. As in that case, the stopped-muon number can be reliably determined from the timing distribution.

Figure 5 (a) shows the two-dimensional histogram of peak timing versus integrated peak value. Two clear loci corresponding to the two beam bunches are again visible. The projection onto the timing axis with an integrated-value threshold of 500 ch is shown in Fig. 5 (b). The fit was performed using the same functional form as in Appendix A.

As in previous cases, the number of stopped muons was extracted by integrating the two Gaussian components corresponding to the muon pulse pair. The estimated number of stopped muons per pulse pair is  $0.581 \pm 0.007$ .

The decay constant obtained from the fit is consistent with the known muon lifetime in both vacuum and carbon. For this configuration, the pileup probability was estimated to be 0.5%, and the corresponding correction was applied, resulting in  $n_{\text{out}} = 0.584 \pm 0.007$ .

### 4. $n_{\text{in}}$ for the 18.0 MeV/c run with a 27- $\mu$ m target

The determination of  $n_{\text{in}}$  for the 18.0 MeV/c run with the 27- $\mu$ m target was performed in the same manner as for the 21.5 MeV/c target-in case, using the timing distribution of peaks identified in the plastic scintillator waveform. Figure 6 summarizes the result.

Compared to the 21.5 MeV/c run, the lower beam momentum in this setting leads to further reduction in muon energy deposition in the scintillator. As a result, the separation between muon and decay-electron signals becomes even less distinct, both in the two-dimensional histogram and in the projected timing distribution. Nevertheless, the stopped-muon yield can be reliably determined from the timing distribution, as in the previous cases.

Figure 6 (a) shows the two-dimensional histogram of peak timing versus integrated waveform value. The muon loci are not clearly distinguishable from the background of decay electrons. As in previous cases, a threshold of 300 ch on the integrated value was applied to suppress low-energy background, and the timing distribution of the selected peaks is shown in Fig. 6 (b).

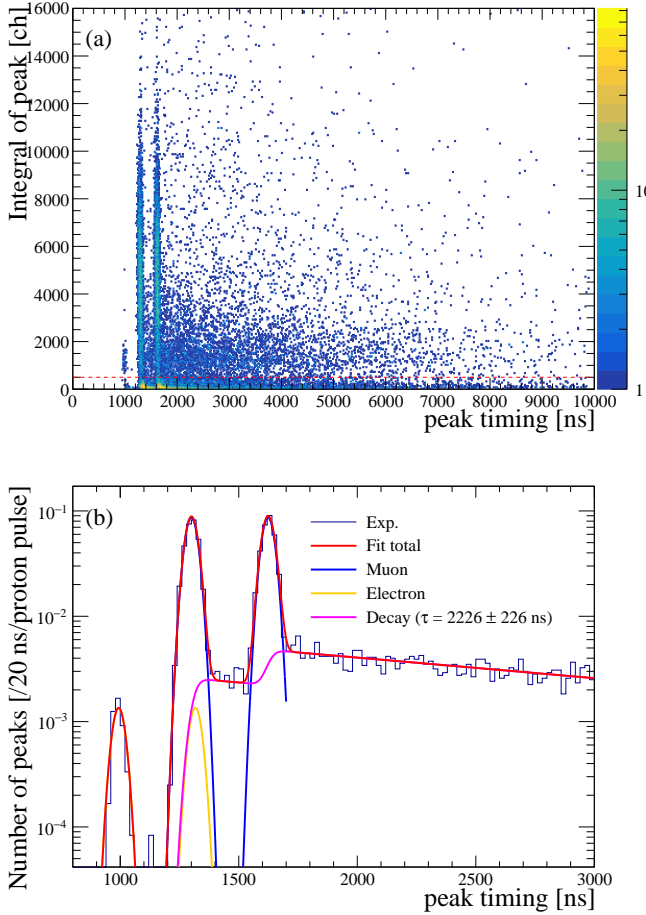


FIG. 5. Beam timing structure for the 18.0 MeV/c run with the target removed. (a) Two-dimensional histogram of peak timing versus integrated waveform value. The applied threshold on the integrated value is indicated by the red dashed line. (b) Timing distribution of peaks after applying an integrated-value threshold of 500 ch. The distribution is fitted using the model described in Appendix A.

The distribution was fitted using the same functional form described in Appendix A. The number of stopped muons was evaluated by integrating the Gaussian components corresponding to the muon pulses. The resulting number of stopped muons per pulse pair is  $n_{\text{in}} = 0.247 \pm 0.005$ .

The decay constant extracted from the exponential component is  $\tau = (1,500 \pm 121)$  ns, which is again consistent with a mixture of muon decays in both silicon and carbon. Given the relatively low muon rate per pulse, the probability of pileup is negligible.

##### 5. Evaluated numbers of stopped muons in the target

Table IV summarizes the evaluated number of incident muons per pulse pair,  $n_{\text{out}}$ , the number of muons stopped

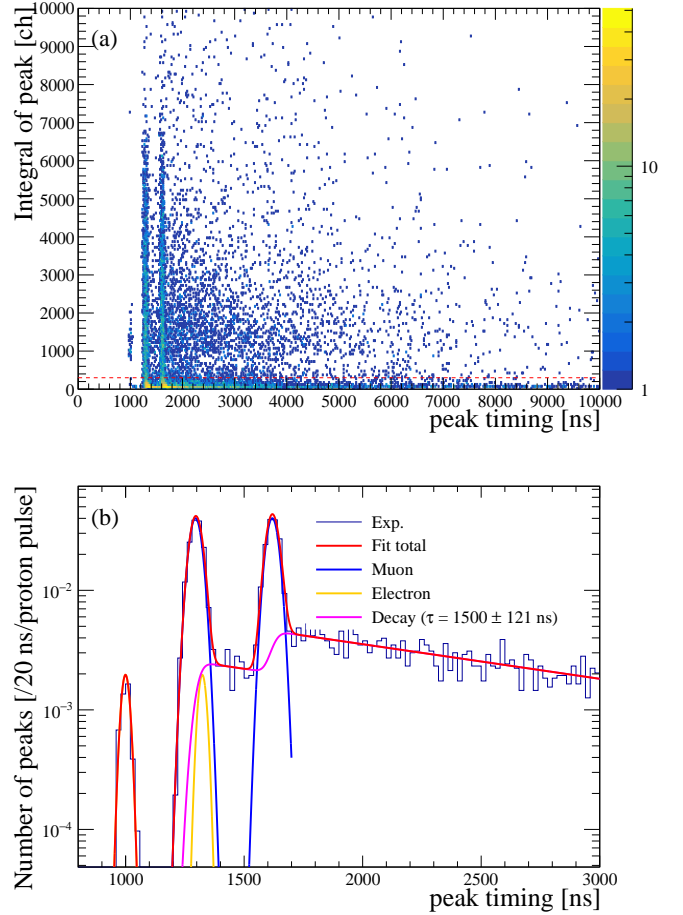


FIG. 6. Analysis of the peak timing distribution for the 18.0 MeV/c run with the target in place. (a) Two-dimensional histogram of peak timing versus integrated waveform value. Due to energy loss in the target and lower beam momentum, the muon loci are less distinct. The applied threshold on the integrated value is indicated by the red dashed line. (b) Timing distribution of peaks after applying an integrated-value threshold. The distribution is fitted using the model described in Appendix A.

TABLE IV. Evaluated muon counts per pulse pair ( $n$ ) and total stopped muon counts in the target for each beam momentum.

$p_{\text{beam}}$ (MeV/c)	$n_{\text{out}}$	$n_{\text{in}}$	$N_{\text{stop}}$ ( $/10^6$ )	$N_{\text{capture}}$ ( $/10^6$ )
21.5	4.080(20)	0.182(6)	16.43(9)	10.68(5)
18.0	0.584(7)	0.267(6)	1.51(4)	1.00(3)

in the plastic scintillator per pulse pair,  $n_{\text{in}}$ , and the total number of muons stopped in the target,  $N_{\text{stop}}$ , for each beam momentum. The values of  $N_{\text{stop}}$  were calculated using Eq. (2).

## B. Energy calibration

The energy signals from the silicon detectors were extracted from the raw waveform data using the same digital pulse-shape analysis (DPSA) method as described in Ref. [26]. For energy calibration of the silicon channels, a mixed  $\alpha$ -source containing  $^{148}\text{Gd}$ ,  $^{241}\text{Am}$ , and  $^{244}\text{Cm}$  was used.

The CsI(Tl) detectors exhibit a non-linear relationship between the light output and deposited energy. Therefore, the quadratic calibration formula were adopted:

$$E = a + bQ + c(bQ)^2 \quad (3)$$

where  $Q$  is the light output. The parameters  $a, b, c$  were determined in two steps:

1. Using measured proton energy loss data in the  $\Delta E$  silicon detectors, we first obtained the corresponding light output  $Q_p$  in the CsI(Tl).

2. We then simulated the proton energy loss  $\Delta E$  in the silicon detector and the residual energy deposited in the CsI(Tl) with Geant4 [29–31], and matched the simulated  $(\Delta E, Q_p)$  pairs to the measured ones.

Figure 7 shows the correlation between  $\Delta E$  and  $Q$  for both the measured data and the Geant4 simulation, demonstrating good agreement over the full dynamic range.

With these calibrations in place, all subsequent energy spectra of charged particles were converted from raw pulse heights into physical energy deposits.

## C. Particle identification

### 1. Telescope TM and TH

For events in which particles penetrated the front Si detectors of telescopes TM and TH, particle identification was performed using the conventional  $\Delta E$ - $E$  method. Figure 7 shows the correlation between the energy deposited in the Si detector and that in the CsI(Tl) scintillator, where clear separation of particle species is achieved up to about 50 MeV. In the present analysis, protons, deuterons, and tritons were identified by requiring that their energy loss in the Si detector fall within  $\pm 3\sigma$  of the centroid values obtained from Geant4 simulations. A population of events attributed to signals from decay electrons or gamma rays is observed in the low-energy region, and these events were not used in the present analysis.

For particles that stopped in the Si detectors, complementary information from telescope TL, which is described in the following subsection, indicates that the yields of  $^3\text{He}$ ,  $^6\text{He}$ , and particles with  $Z > 2$  are negligible compared to alpha particles. Accordingly, events exhibiting an energy loss above 13 MeV, corresponding to the penetration threshold of tritons through all Si detectors, were identified as alpha particles.

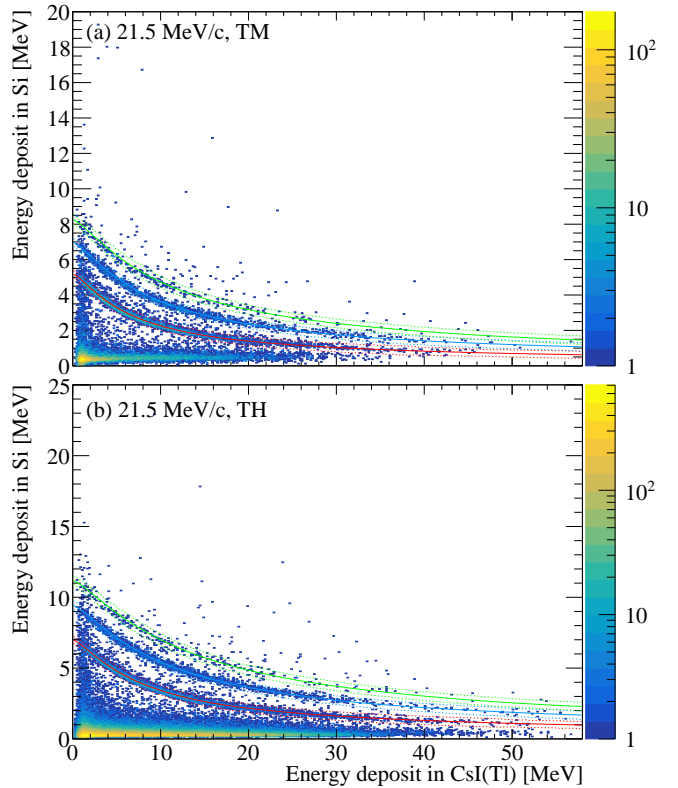


FIG. 7. (a)  $\Delta E$ - $E$  plot obtained with telescope TM for a muon beam momentum of 21.5 MeV/c. The horizontal axis represents the energy deposited in the CsI(Tl) scintillator, while the vertical axis shows the energy deposited in the Si detector. The solid lines indicate the centroid loci of the Geant4 simulations, and the dashed lines correspond to  $\pm 3\sigma$  around them. Events within these bands were selected as the respective particle species: protons (red), deuterons (blue), and tritons (green). (b) Same as (a), but for telescope TH.

### 2. Telescope TL

Particle identification in telescope TL was performed using the digital pulse shape analysis method described in Ref. [26]. Figure 8 shows the correlation between the energy deposited in the nTD-Si detector and the maximum current ( $I_{\max}$ ). Since the statistics of the 27- $\mu\text{m}$  target run were limited, graphical cuts were defined using the 200- $\mu\text{m}$  target data and subsequently applied to the 27- $\mu\text{m}$  data. An intense component is observed in the low-energy region, which is attributed to signals induced by decay electrons or gamma rays; this component was not used in the present analysis and does not affect the results discussed below.

Below 2 MeV, particle separation was not feasible with this method; however, given that protons dominate the energy spectrum in this region, all particles with energies below 2 MeV were treated as protons in the analysis, as shown in Fig. 8. Similarly, in the 2–3 MeV region, deuterons, tritons, and alpha particles could not be distinguished. In this case, non-proton particles were

treated as alpha particles for the same reason.

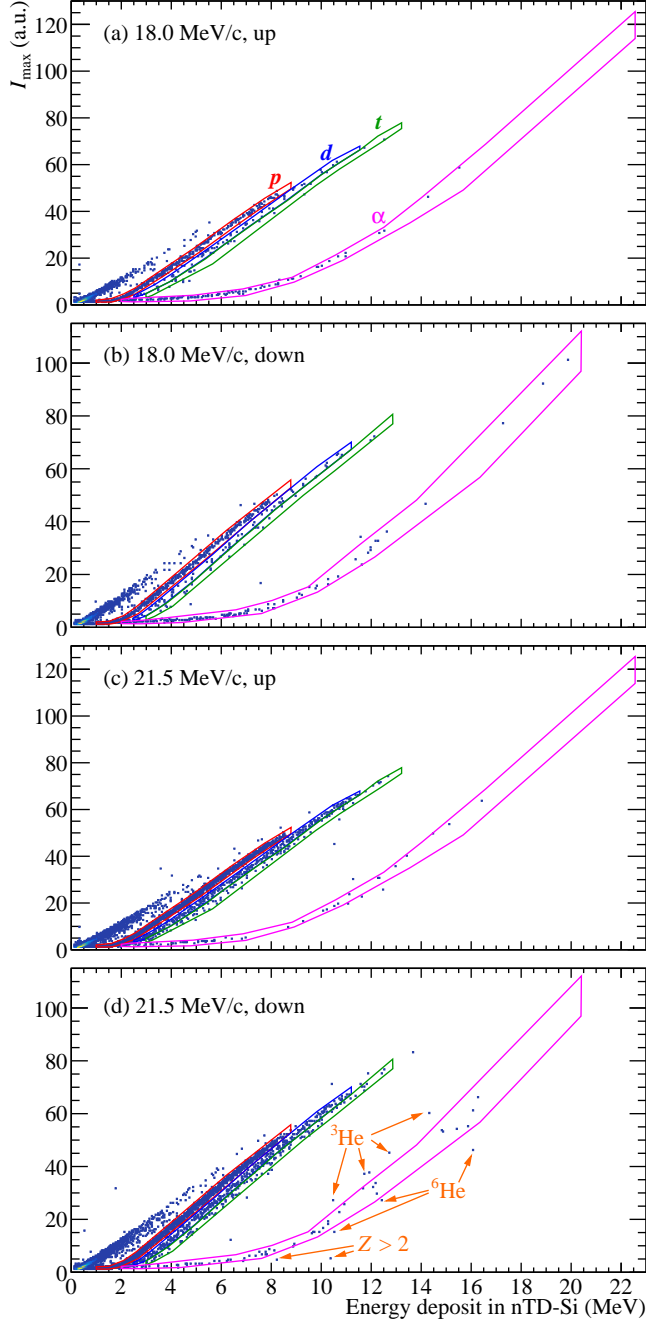


FIG. 8. Particle identification plots obtained using digital pulse-shape analysis (DPSA) with telescope TL. Panels (a) and (b) show the results for an incident muon momentum of  $18.0 \text{ MeV}/c$  with the detector placed at the upper ( $\alpha = +45^\circ$ ) and lower ( $\alpha = -45^\circ$ ) positions relative to the target, respectively. Panels (c) and (d) show the corresponding results for  $21.5 \text{ MeV}/c$ . The correlation between the energy deposited in the nTD-Si detector and the maximum current ( $I_{\max}$ ) is shown. The loci of protons (red), deuterons (blue), tritons (green), and  $\alpha$  particles (magenta) are indicated. Events corresponding to rare charged-particle emission channels ( ${}^3, {}^6\text{He}$  and  $Z > 2$ ) are indicated by orange arrows.

In the  $200\text{-}\mu\text{m}$  run, a few number of events consistent with  ${}^3\text{He}$  or  ${}^6\text{He}$  were observed. However, their statistics were too limited, and the effect of energy loss in the target was too large to extract their energy spectra. In addition, two events attributable to particles with  $Z > 2$  were also observed, possibly corresponding to the emission of heavier clusters such as  ${}^8\text{Be}$ . To the best of our knowledge, such observations of  ${}^3\text{He}$ ,  ${}^6\text{He}$ , and  $Z > 2$  cluster emission following  $\mu\text{NC}$  have not been reported previously, and this work therefore represents the first experimental evidence of these channels.

#### D. Event Selection

##### 1. Beam Signal

Waveform acquisition was synchronized with the 50 Hz timing signal of the synchrotron; however, proton beam pulses were delivered to TS1 only at 40 pulses per second. As a result, data were also recorded during periods without proton delivery to TS1. To restrict the analysis to events associated with the incoming muon beam, a co-incident signal from the Cherenkov detector installed in the muon beamline was required. Only events fulfilling this condition were retained for further analysis.

##### 2. Signal Timing

In the present measurement, the waveform record length was set to 20,000 ns, with the external trigger signal fed at 2,000 ns. Throughout this paper, the signal timing is defined relative to this trigger position.

Figure 9 shows the distribution of signal rise times measured with the nTD-Si detector in the TL telescopes, together with the distribution of events identified as protons. The overall distribution exhibits a decay constant of approximately  $2\ \mu\text{s}$ , which is attributed mainly to events where muons stopped in surrounding polyethylene materials such as the beam collimator and the chamber walls. In contrast, the proton distribution yields a decay constant of  $795 \pm 51$  ns, consistent with the muonic atom lifetime in silicon of  $756.0(10)$  ns reported in the literature [28]. This agreement demonstrates that the observed protons originate from  $\mu\text{NC}$  in the Si target.

To retain target-originated events while reducing the contribution from muon stops in non-target materials, the present analysis was restricted to events occurring between 1,400 ns and 6,000 ns. The two muon beam bunches arrive at approximately 1,450 ns and 1,800 ns, respectively. The upper limit of 6,000 ns was chosen so as to cover a time interval corresponding to approximately six lifetimes of the muonic atom in silicon. The resulting loss of genuine target events is estimated to be at most about 0.3%, which is negligible compared to the uncertainty in the number of stopped muons.

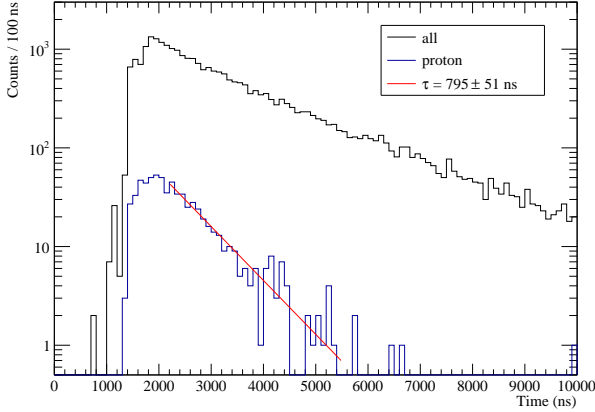


FIG. 9. Distribution of signal rise times measured with the nTD-Si detectors in the TL telescopes for a muon beam momentum of 21.5 MeV/c.

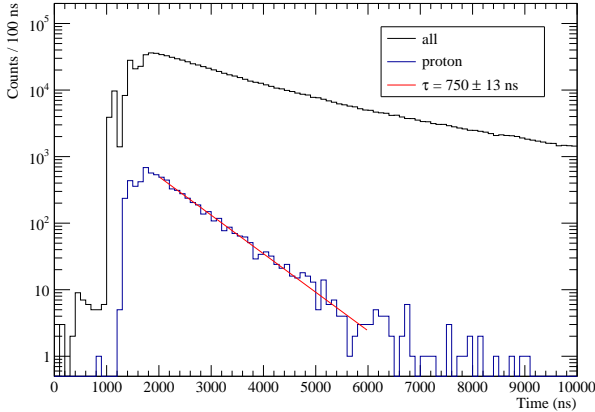


FIG. 10. Distribution of signal rise times measured with the Si detectors in the TH telescopes for a muon beam momentum of 21.5 MeV/c.

The timing distribution measured with the Si detectors in the TH telescopes, together with the distribution of events identified as protons, is shown in Fig. 10. The overall component includes contributions from muons stopped in surrounding materials, while the proton component yields a decay constant of  $750 \pm 13$  ns. This value is consistent with the muonic atom lifetime in silicon reported in the literature [28], confirming that the protons observed in the TH telescopes also originate from  $\mu$ NC in the Si target. For the analysis, events occurring between 1,200 ns and 6,000 ns were selected.

### 3. Time Difference between Si and CsI(Tl) signals

For events in which particles penetrated a Si detector of telescopes TM and TH, an additional selection based

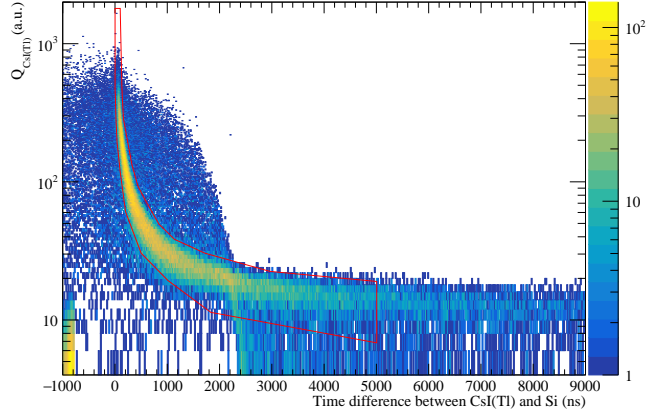


FIG. 11. Correlation plot of the time difference and the integrated charge of the CsI(Tl) signal. The horizontal axis represents the time difference between the rise times of the CsI(Tl) and Si detector signals, while the vertical axis shows the integrated charge ( $Q$ ) of the CsI(Tl) signal. The graphical selection region applied in the analysis is indicated by the red solid line.

on timing information was applied to ensure true coincidences between the Si and CsI(Tl) detectors. The leading time of each waveform was defined as the point where the signal exceeded a threshold set at  $7\sigma$  above the baseline fluctuation. The difference between the leading times of the Si and CsI(Tl) signals was then used as the selection variable.

Figure 11 shows the correlation between this time difference and the integrated charge of the CsI(Tl) signal. A clear dependence is observed: events with lower CsI(Tl) charge exhibit larger time differences, reflecting the effect of time walk. The graphical cut adopted in the analysis is indicated by the red solid line in the figure.

### E. Measured energy spectra

Based on the particle identification methods and event selection procedures described above, the measured energy spectra for each particle species were obtained, as shown in Fig. 12. In the overlapping energy regions covered by different telescopes, the spectra are generally consistent with each other. However, in the overlapping region between TL and TM, the spectrum measured with TM is slightly suppressed compared to that with TL. This suppression is attributed to the relatively thick insensitive layer (20  $\mu$ m according to the datasheet) of the Hamamatsu Si detectors used in TM and TH. The influence of such insensitive layers, as well as energy loss in the target, is corrected for in the unfolding analysis described in the following section.

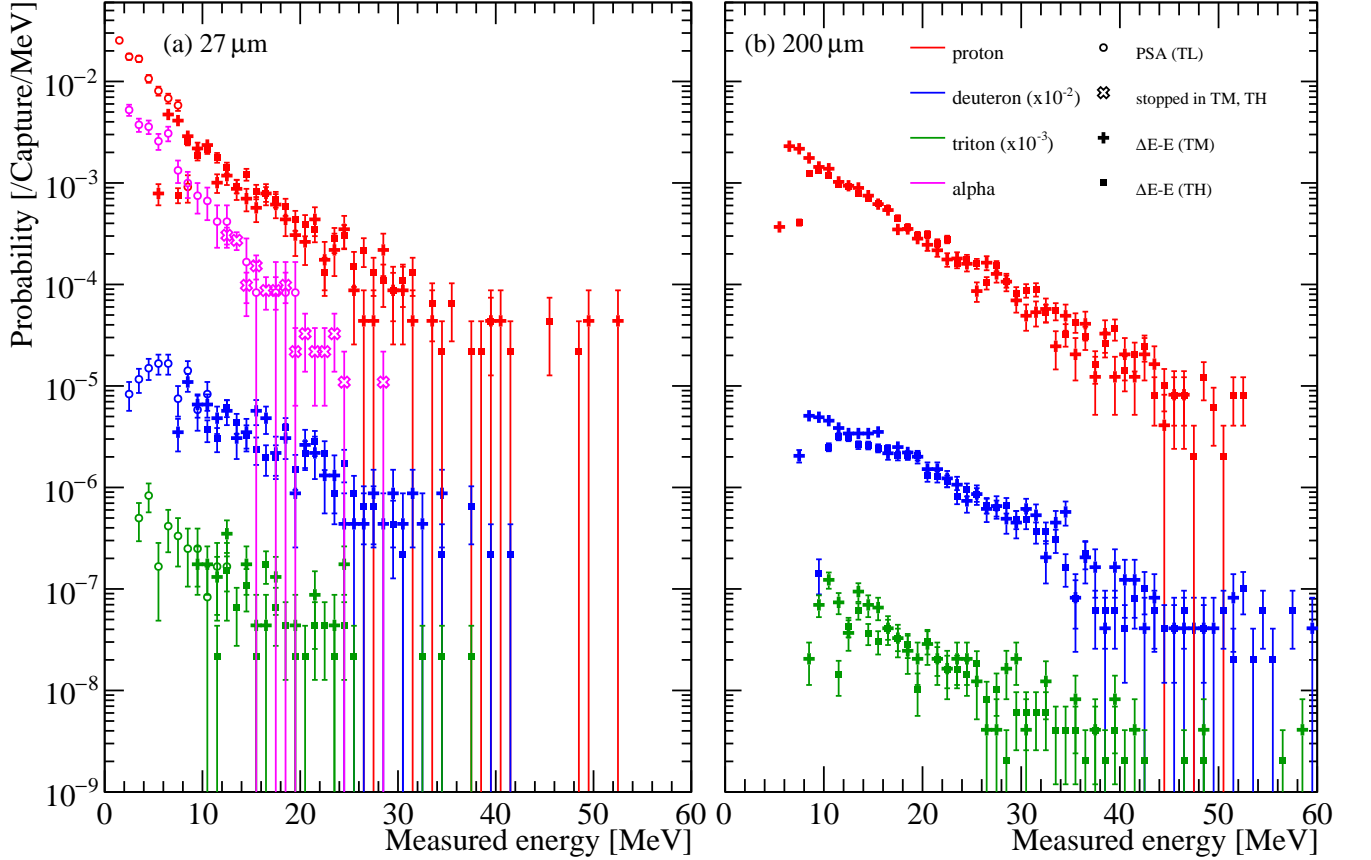


FIG. 12. Measured energy spectra of charged particles emitted following  $\mu$ NC in Si before unfolding analysis with (a) the 27- $\mu$ m target and (b) the 200- $\mu$ m target.

#### F. Unfolding

Energy losses in the target material and in the inactive layers of the detectors distort the measured energy spectra of emitted particles. In order to extract the initial energy spectra at the emission point, an unfolding analysis was performed.

The detector response functions were constructed using Monte Carlo simulations based on Geant4 [29–31], which take into account the full experimental geometry as well as energy loss and straggling effects in the target and inactive layers of the detectors. In these simulations, the initial energies of emitted particles were sampled from a uniform energy distribution covering the full kinematically relevant range for each particle species.

The use of a uniform energy distribution ensures that the response matrices represent purely the detector response and energy-loss effects, without introducing any model-dependent assumptions on the underlying physical energy spectra. The resulting response matrices therefore describe the probability of observing a given measured energy for a particle emitted with a certain initial energy, independent of the assumed emission model.

In the unfolding procedure, the detector response functions were weighted according to the three-dimensional muon stopping-position distribution inside the target. The stopping-position distribution was estimated using dedicated simulations using G4beamline [32], which model the transport and energy loss of the incident muon beam in the experimental setup. The initial beam profile and momentum distribution in the simulation were tuned to reproduce the measured beam characteristics reported in Ref. [24]. In addition, the central momentum of the muon beam was adjusted such that the simulated stopping ratio reproduces the experimentally measured value in the present experiment. The weighted response functions thus account for the realistic spatial distribution of muon stopping positions within the target.

The unfolding was carried out using the `RooUnfold` unfolding framework [33], employing the iterative Bayesian unfolding method [34] implemented in the `RooUnfoldBayes` class. The number of iterations was set to the default value of four.

Measured energy spectra obtained with different target thicknesses (27  $\mu$ m and 200  $\mu$ m) and with multiple detector telescopes were included simultaneously in a single unfolding procedure. Each data set was described by its

corresponding response function, while a common initial energy spectrum was assumed.

Statistical uncertainties of the unfolded spectra were evaluated using a toy Monte Carlo approach. A set of 10 000 pseudo-data spectra was generated by fluctuating the measured spectra according to Poisson statistics in each energy bin. The unfolding procedure was applied to each pseudo-data set, and the resulting distribution of unfolded spectra was used to estimate the statistical uncertainties. Systematic uncertainties associated with the unfolding procedure are discussed in the following subsection.

## G. Systematic uncertainties

### 1. Number of stopped muons

The uncertainty in the number of stopped muons constitutes a source of systematic uncertainty in the absolute normalization of the unfolded spectra. In the present analysis, the unfolding was performed simultaneously using data sets obtained with different target thicknesses and detector configurations, which is expected to reduce the sensitivity to the uncertainty in the stopped-muon determination.

Nevertheless, a conservative estimate was adopted. For the 18.0 MeV/c run with the thin target, a relative uncertainty of 3% was assigned based on the determination of the number of stopped muons. For the 21.5 MeV/c run, an independent relative uncertainty of 3% was assigned to account for the pileup correction applied in the stopped-muon determination. Although these uncertainties originate from independent sources, their impact on the final results was conservatively taken to be 3%. This normalization uncertainty was propagated to the final results.

### 2. Detector placement

Uncertainties in the relative positioning of the detectors and the target constitute a source of systematic uncertainty in the measured yields. Taking into account possible mechanical tolerances in the experimental setup, relative misalignments of the order of 1 mm in any direction cannot be excluded.

The effect of such misalignments on the overall yields was evaluated, and the resulting systematic uncertainty was estimated to be 2.4%. This uncertainty was applied as an overall normalization uncertainty in the analysis.

### 3. Unfolding procedure

Systematic uncertainties associated with the unfolding procedure were evaluated by varying key inputs to the

response matrix and by assessing the stability of the unfolding with respect to the number of iterations.

First, the sensitivity to the muon stopping distribution inside the target was investigated. Starting from the response matrices constructed using the tuned muon beam conditions that reproduce the experimentally measured stopping ratio, the unfolding was repeated using response matrices obtained from simulations in which the incident muon momentum was varied such that the mean stopping position of muons inside the target was shifted along the beam axis by  $\pm 10\%$  of the target thickness. The resulting changes in the unfolded spectra were found to be negligible compared to the corresponding statistical uncertainties and were therefore not included as an additional systematic contribution.

The thicknesses of the Si targets were measured using a micrometer. The observed variation was smaller than the instrumental resolution of 1  $\mu\text{m}$ . This level of uncertainty is negligible for the present analysis and is effectively absorbed into the uncertainty associated with the muon stopping distribution inside the target.

Second, the dependence on the number of iterations in the iterative Bayesian unfolding was examined. The unfolded spectra were found to be well converged, with bin-by-bin differences between the results obtained with 4 and 20 iterations remaining within 3% for most energy bins. These differences were taken as a conservative estimate of the systematic uncertainty associated with the unfolding procedure.

### 4. Energy calibration

Systematic uncertainties associated with the energy calibration were evaluated by assessing the impact of plausible variations in the energy scale on the unfolded spectra.

For telescope TL, the energy calibration uncertainty was conservatively estimated by introducing an offset of  $\pm 100\text{ keV}$  combined with a scaling uncertainty of  $\pm 1\%$ . These variations account for possible residual uncertainties in the offset and gain determination of the nTD-Si detector.

For telescopes TM and TH, the energy calibration uncertainty was conservatively estimated by applying a uniform scaling variation of  $\pm 3\%$  to the reconstructed energies. This choice reflects the dominant uncertainty associated with the energy response of the CsI(Tl) scintillator and possible nonlinearity effects.

The analysis was repeated after applying these energy-scale variations, and the resulting changes in the spectra and extracted observables were taken as systematic uncertainties associated with the energy calibration.

## IV. RESULTS

Figure 13 shows the initial energy spectra of emitted protons, deuterons, tritons, and  $\alpha$  particles obtained in the present experiment. For all four particle species, energy spectra were successfully extracted over a wide energy range, extending from the low-energy region up to several tens of MeV, demonstrating the broad kinematic coverage achieved in this measurement.

The error bars shown in Fig. 13 represent the uncertainties propagated through the unfolding procedure. While these uncertainties are dominated by statistical errors of the measured spectra, the unfolding process introduces correlations between neighboring energy bins, and therefore the uncertainties should not be regarded as strictly independent point by point.

As a global feature common to all particle species, the emission probabilities decrease approximately exponentially with increasing emission energy. This overall behavior is qualitatively consistent with the generic characteristics expected for particle emission following  $\mu$ NC.

Coulomb-barrier effects are expected to cause a drop-off in the emission probability at low energies, with a preceding flattening of the spectral slope. In the present measurement, a slight flattening is seen only in the  $\alpha$ -particle spectrum, but the limited low-energy coverage prevents any quantitative assessment.

At the same time, noticeable differences are observed in the spectral slopes among protons, deuterons, tritons, and  $\alpha$  particles. These differences indicate that the energy distributions depend on the type of emitted particle, suggesting that the underlying emission processes are not universal but instead reflect intrinsic differences associated with the emission mechanism and particle properties.

## V. DISCUSSION

### A. Energy spectra

#### 1. Comparison with previous experiments

Figure 13 compares the initial energy spectra obtained in the present work with all previously published experimental data [18–20] on charged particle emission following  $\mu$ NC on Si.

Overall, the present measurement provides charged-particle energy spectra over a significantly broader energy range than any of the previous experiments. In particular, continuous coverage is achieved from the low-energy region up to several tens of MeV for protons, deuterons, and tritons, demonstrating the comprehensive nature of the present dataset.

In comparison with the data reported by Budyashov *et al.* [18], the present spectra exhibit a systematic deviation in the high-energy region, where the Budyashov

data show anomalously large emission probabilities. This discrepancy may be related to effects such as energy loss or distortion in the target material; however, detailed information on the data analysis procedures is not provided in the original publication, and the origin of the discrepancy therefore remains unclear.

The spectra reported by Manabe *et al.* [20] exhibit good overall agreement with the present results in terms of spectral shape over the energy range where the datasets overlap. The absolute yields reported in Ref. [20] are, however, systematically slightly higher than those obtained in the present work. This difference is most likely attributable to the normalization procedure adopted in Ref. [20], where the spectra were normalized to the 17 MeV proton data [18] reported by Budyashov *et al.* Despite this difference in normalization, the overall spectral behavior is consistent between the two measurements.

Among the existing data, the spectra reported by Edmonds *et al.* [19] represent the most comprehensive prior measurement in terms of particle species and energy coverage. The present results are in good agreement with these data for protons, deuterons, and tritons over most of the overlapping energy range. A small systematic difference is observed in the low-energy region of the proton spectrum, where the yields reported by Edmonds *et al.* are slightly higher than those obtained in the present work. This difference may be related to a possible energy offset in the calibration, for example arising from differences in the treatment of insensitive layers in the detector telescopes. In Ref. [19], the treatment of the energy calibration uncertainty focused on the overall energy scale, while a potential offset component was not discussed explicitly.

A key advancement of the present work is the extension of the  $\alpha$ -particle spectrum toward significantly lower energies than previously achieved, providing new experimental constraints on the low-energy evaporation component.

#### 2. Comparison with theoretical model calculations

To interpret the measured charged-particle energy spectra, the present results are compared with representative theoretical model calculations. In the following, we focus on two approaches that have been applied to describe particle emission following  $\mu$ NC: the microscopic and evaporation model (MEM) by Minato *et al.* [35], and the particle transport code PHITS [36].

The MEM calculation [35] described particle emission following  $\mu$ NC as a three-step process that explicitly incorporates nuclear many-body effects. In the first step, the weak one-body operators associated with muon capture [37] excites the nucleus and generates particle-hole configurations in the daughter nucleus. In Ref. [35], this initial excitation was treated using the second Tamm-Dancoff approximation (STDA) [38], which

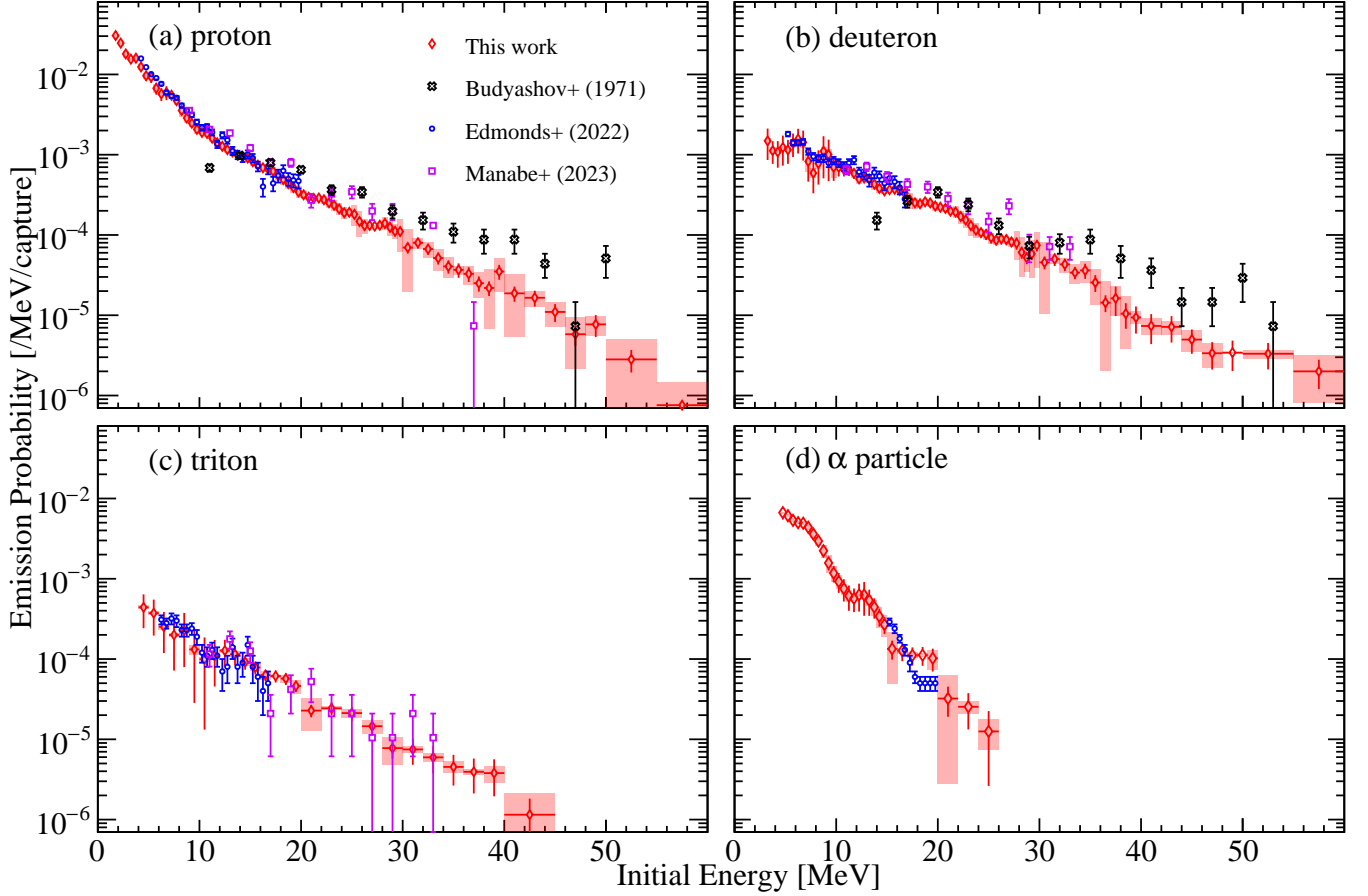


FIG. 13. Initial energy spectra obtained in this work for (a) protons, (b) deuterons, (c) tritons, and (d)  $\alpha$  particles, compared with preceding experimental data [18–20]. The shaded areas represent systematic uncertainties associated with the unfolding iterations and the energy calibration, while overall normalization uncertainties from the muon number determination and detector alignment are not included.

incorporates two-particle-two-hole (2p-2h) configurations through the coupling of one-particle-one-hole (1p-1h) and 2p-2h states. Although Ref. [35] employed both SkO' [39] and SGII [40], the present calculations were performed using SkO' only. The dependence of the charged-particle energy spectra on the choice of these effective interactions was found to be weak. This extension allows us to examine the sensitivity of the strength distributions to the treatment of nuclear correlations over a wide excitation-energy range. In addition to the one-body weak interaction, the effect of meson-exchange currents (MEC) [41] is incorporated phenomenologically. MEC-induced transitions are treated as an additional contribution to the initial excitation, enhancing the population of high-energy configurations that are not sufficiently described by one-body operators alone. This contribution is particularly important for reproducing the high-energy components of proton emission spectra [35].

In the second step, the subsequent de-excitation is modeled within the framework of the two-component exciton model [42, 43]. This model describes the evolution from the initially populated particle-hole configu-

rations toward statistical equilibrium, allowing for preequilibrium emission of nucleons and light clusters during the equilibration process. Once a compound-nuclear configuration is formed, the remaining excitation energy is dissipated through statistical evaporation, treated using a Hauser-Feshbach formalism [44, 45].

In contrast, PHITS [36] is a general-purpose Monte Carlo particle transport code designed to simulate the production, interaction, and transport of a wide variety of particles over a broad energy range. As part of its comprehensive physics framework, PHITS includes models for muon-induced reactions [46], which enable simulations of processes following muon capture, such as preequilibrium emission and statistical evaporation. In the muon capture module of PHITS, the excitation energy of the nucleus after  $\mu$ NC is sampled from the phenomenological excitation function proposed by Singer [47], rather than being derived from an explicit microscopic description of nuclear structure. Particle emission following  $\mu$ NC is then modeled using a combination of the JAERI quantum molecular dynamics (JQMD) model [48, 49] for the preequilibrium stage and the General Evaporation

Model (GEM) [50, 51] for subsequent statistical decay, with parameters constrained by a broad range of experimental data. In addition, to enhance the emission of light composite particles, PHITS incorporates a surface coalescence model (SCM) [52], which accounts for the formation of composite particles through the coalescence of emitted nucleons near the nuclear surface. PHITS provides an event-by-event description of particle production and transport, allowing direct comparison with experimental observables such as energy spectra and particle yields.

In the present study, calculations were performed not only with the standard PHITS models but also with an extended treatment that phenomenologically incorporates the MEC effect [41], in close analogy to the MEM-based approach. This extension enhances the population of high-excitation-energy configurations following  $\mu$ NC and allows us to assess the impact of MEC on emitted-particle spectra within the PHITS framework.

Both models have been shown to reproduce global features of charged-particle emission following  $\mu$ NC, such as overall yields and general spectral trends. However, they rely on different assumptions regarding the treatment of preequilibrium dynamics and the formation of composite particles. A comparison between the present data and these model calculations therefore provides valuable insight into the mechanisms governing charged-particle emission, as well as into the limitations of existing theoretical descriptions.

Figure 14 compares the experimentally obtained initial energy spectra with the MEM calculations. The calculated spectra are further decomposed into contributions from STDA and MEC, each of which is separated into preequilibrium and evaporation components. Overall, the MEM calculation reproduces the global features of the measured spectra reasonably well for all particle species. At the same time, a more detailed comparison reveals systematic deviations that depend on the particle type and the energy region.

For protons, the inclusion of the MEM component is essential to reproduce the high-energy part of the preequilibrium emission. A more detailed comparison reveals systematic deviations that depend on the energy region. The MEM calculation tends to overestimate the yield in the low-energy region, while underestimating the emission probability in the intermediate energy range of approximately 10–20 MeV. In the high-energy region, the calculated spectrum decreases more slowly than the experimental one, resulting in a slight overestimation of the yield. These features suggest that, while the present two-component description consisting of preequilibrium and compound contributions captures the gross behavior, a more refined treatment of the transition between different emission mechanisms may be required.

For deuterons and tritons, the overall agreement between the experimental data and the MEM calculation is reasonably good over a wide energy range, indicating that the description of composite particle emission

within the Iwamoto-Harada model [53, 54] captures the essential features of deuteron and triton emission following  $\mu$ NC. In contrast to the proton case, the contribution from MEC is found to be less pronounced for these composite particles. For deuterons, a slight underestimation is observed in the high-energy region. For tritons, on the other hand, the calculated yield tends to be systematically larger than the experimental data, although the overall spectral shape is well reproduced. These discrepancies suggest that further refinement of the preequilibrium component would be required for a more quantitative description.

In contrast, the comparison for  $\alpha$  particles reveals a more pronounced energy-dependent discrepancy. The low-energy part of the  $\alpha$  spectrum is well reproduced by the MEM calculation, indicating that the evaporation component, which dominates this energy region, provides an adequate description of low-energy  $\alpha$  emission. However, at energies above 10 MeV, the MEM calculation significantly overestimates the measured  $\alpha$  yield. This discrepancy suggests limitations in the current treatment of composite particle formation within the Iwamoto-Harada model [53, 54] for  $\alpha$  emission, particularly in the high-energy region where non-evaporative processes are expected to contribute. The present results therefore point to the need for further refinement of the model, in particular with respect to the description of composite particle formation and preequilibrium  $\alpha$  emission.

Figure 15 shows a comparison of the experimental initial-energy spectra with PHITS calculations. Results obtained with the original PHITS model and with extensions including the SCM and MEC effects are shown. For the PHITS calculation including both the SCM and MEC effects (PHITS+SCM+MEC), the breakdown into preequilibrium and evaporation components is also presented. Overall, the inclusion of both the SCM and MEC effects leads to an improved description of the measured spectra for all charged particle species, although noticeable particle-dependent discrepancies remain.

For protons, the overall spectral shape is reproduced at a level comparable to that obtained with the MEM calculations. Both MEM and PHITS exhibit a similar overestimation in the low-energy region, as well as discrepancies in the intermediate-energy range of 10–20 MeV. The original PHITS model alone shows a significantly poorer agreement with the data, indicating that the inclusion of the MEC effect is essential for achieving a reasonable reproduction of the proton spectrum.

For deuterons and tritons, the low-energy peak is reproduced to some extent, whereas the high-energy components are significantly underestimated. Although the inclusion of SCM and the MEC effect substantially improves the overall agreement, particularly at low energies, noticeable discrepancies persist in the high-energy region. The agreement achieved by the PHITS calculations is therefore not yet fully comparable to that obtained with the MEM calculations.

For  $\alpha$  particles, the agreement between the experimen-

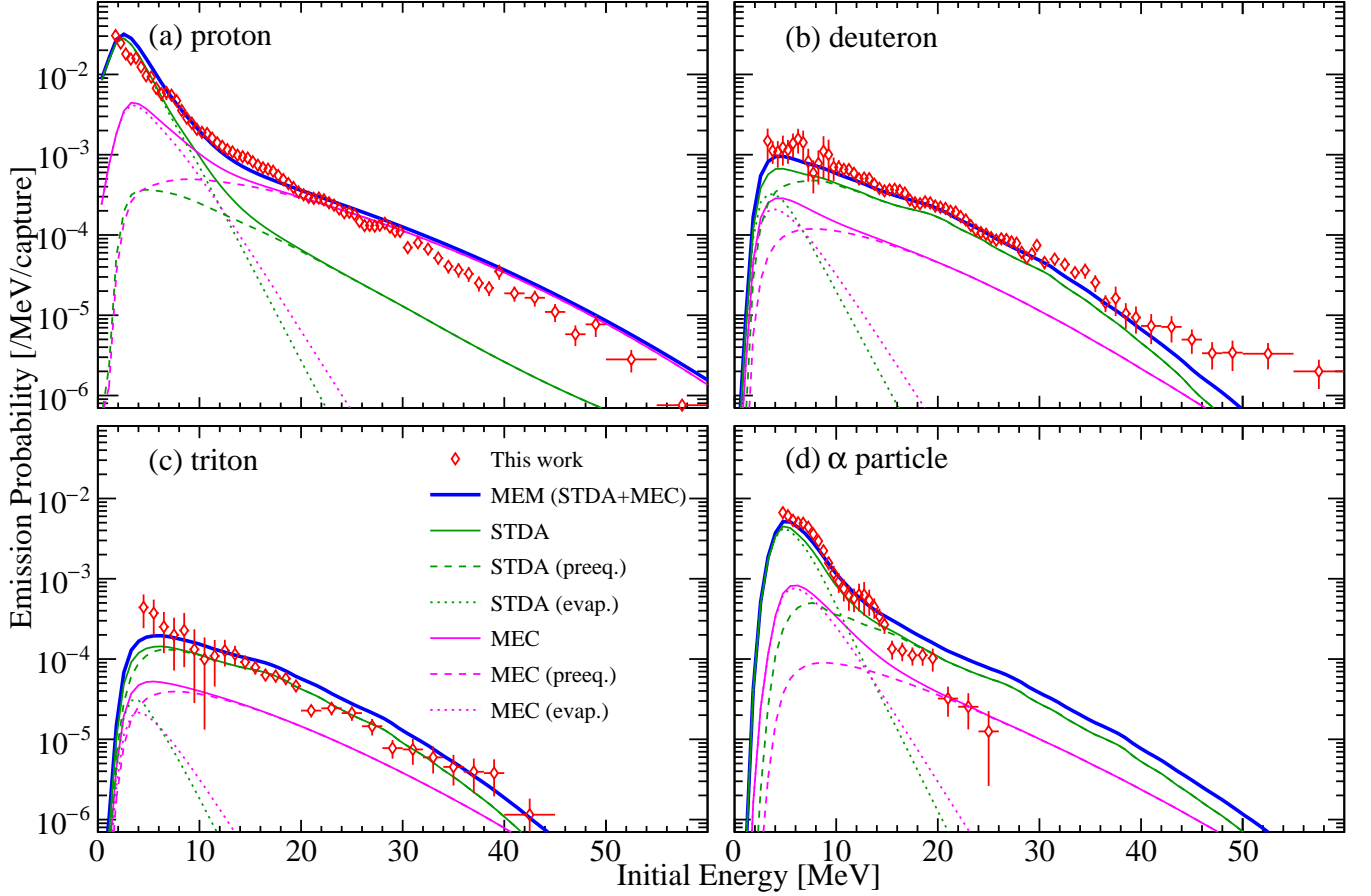


FIG. 14. Initial energy spectra obtained in this work for (a) protons, (b) deuterons, (c) tritons, and (d)  $\alpha$  particles. The experimental data are compared with MEM calculations [35] performed using the SkO' effective interaction. In the MEM calculations, the total spectra are decomposed into contributions from the initial excitation described by the STDA and from the MEC component. Each of these contributions is further separated into preequilibrium and evaporation components.

tal data and the calculations shows a pronounced energy dependence. At lower energies, where the evaporation component dominates, the yield is overestimated. In contrast, in the high-energy region above approximately 15 MeV, where the preequilibrium component becomes dominant, the PHITS+SCM+MEC calculations reproduce the high-energy behavior more successfully than the MEM calculations. These results indicate that further refinement in the modeling of  $\alpha$ -particle emission following  $\mu$ NC is required, particularly in the evaporation-dominated low-energy region.

Overall, the comparisons with the MEM and PHITS calculations indicate that the level of agreement depends on both the particle species and the modeling approach. While proton spectra are reproduced reasonably well by both models, noticeable differences emerge for composite particles, reflecting a pronounced particle-species dependence in the modeling of charged-particle emission.

## B. Charged particle yields

### 1. Comparison with previous experiments

A comparison of the integrated yields of emitted charged particles obtained in the present work with previous measurements by Edmonds [19] and Sobottka and Wills [17] is summarized in Table V. Since the present measurement covers a wider energy range than the previous studies, the integrated yields shown in Table V are evaluated over the same energy intervals as those adopted in the corresponding reference data, in order to enable a direct comparison.

For  $Z = 1$  charged particles, the integrated yields obtained in the present work are systematically smaller than those reported by Edmonds [19]. As discussed in Sec. V A 1, this difference may be attributed to systematic effects in the low-energy region of the spectra, where the treatment of energy calibration and energy-loss corrections is particularly sensitive.

For  $\alpha$  particles, the integrated yields obtained in the present work are consistent with those reported by Ed-

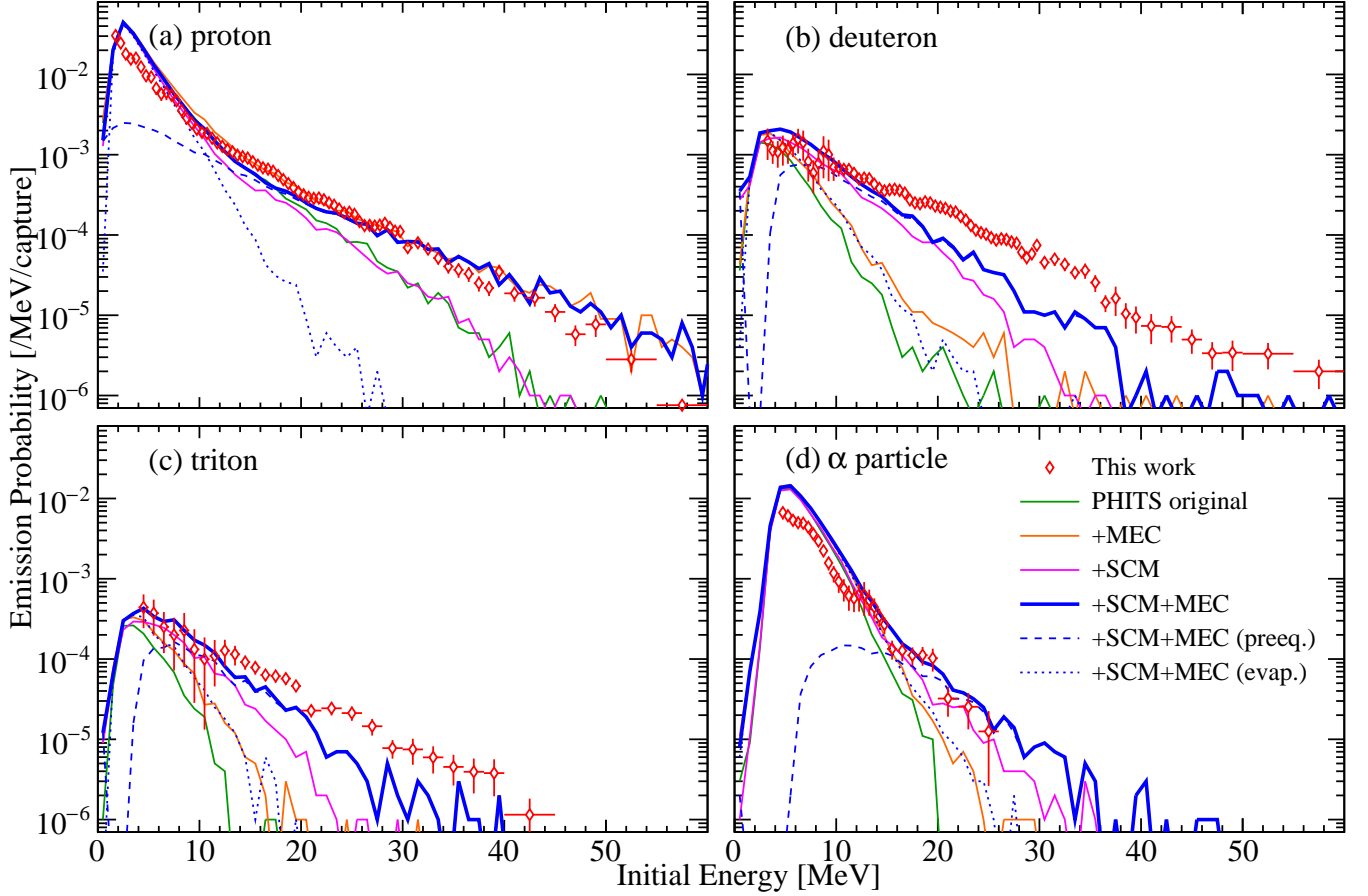


FIG. 15. Initial energy spectra obtained in this work for (a) protons, (b) deuterons, (c) tritons, and (d)  $\alpha$  particles, compared with PHITS calculations using the original model (PHITS), with SCM (+SCM) and with the MEC extension (PHITS+MEC), and with both extensions (+SCM+MEC). For the PHITS+SCM+MEC calculations, the total spectra are shown together with the separate contributions from the preequilibrium (preeq.) and evaporation (evap.) processes.

monds [19] within the quoted uncertainties. This agreement is likely due to the fact that the  $\alpha$ -particle energy range covered in Ref. [19] is sufficiently high that the results are largely insensitive to systematic effects associated with energy calibration in the low-energy region.

## 2. Comparison with theoretical model calculations

Table V also compares the results with theoretical model calculations. The theoretical values considered here are taken from the work of Lifshitz and Singer [55], which provides both inclusive and exclusive predictions for charged-particle emission following  $\mu$ NC in  $^{28}\text{Si}$ , as well as from the MEM calculations [35] discussed in the previous section.

First, the present results are compared with the calculations by Lifshitz and Singer [55]. In that work, theoretical predictions are provided only for protons, deuterons,  $\alpha$  particles, and the total charged-particle yield.

For proton emission, the exclusive theoretical yield is smaller than the experimentally determined integrated

yield. However, this difference does not necessarily indicate an inconsistency, since the exclusive calculation corresponds to proton emission without accompanying neutron emission, whereas the experimental yield includes contributions from channels in which protons are emitted in coincidence with one or more neutrons. For deuteron and  $\alpha$  emission, the inclusive theoretical yields appear to be somewhat larger than the corresponding experimental values.

For the total charged-particle yield, the theoretical value is comparable to the experimentally determined lower limit. Given the limited coverage of the charged-particle spectrum in the experiment, particularly at low energies, the calculation may underestimate the total charged-particle yield to some extent. Nevertheless, considering the age of the calculation and the simplified treatment of particle emission available at the time, the overall level of agreement can be considered quite good.

The experimental results are next compared with the MEM calculations [35]. For proton emission, the calculated yield significantly exceeds the experimental result. As discussed in Sec. V and illustrated in Fig. 14, this dis-

TABLE V. Comparison of integrated yields of emitted charged particles (in  $10^{-3}$  per capture) following  $\mu$ NC on silicon. The present results are compared with previous direct measurements, theoretical calculations, and branching ratios deduced from activation measurements of  $\mu$ NC in  $^{28}\text{Si}$ . The theoretical values from Ref. [55] correspond to either inclusive or exclusive emission, as specified. For the direct measurements, the yields are integrated over the energy ranges indicated in brackets in MeV. For the activation data, the corresponding residual nuclei and reaction channels are listed.

emitted particle	Direct measurements				Theory	Activation measurements		
	This work	Edmonds [19]	Sobottka-Wills [17]	Lifshitz-Singer [55]	MEM(SkO') [35]	residual nucleus	decay channel	Mizuno [6]
$p$	99.6(27)(38)	—	—	32	144	$^{27}\text{Mg}$	$0n1p$	28.7(17)
	[1.5 $\leq$ $E$ $\leq$ 60]	—	—	(exclusive)	—			
$d$	44.9(15)(17)	52.5(6)(18)	—	21	11.2	$^{26}\text{Mg}$	$1n1p$	> 84(8)
	[4 $\leq$ $E$ $\leq$ 20]	—	—	(inclusive)	8.2			
$t$	13.4(8)(5)	—	—	—	—	$^{25}\text{Mg}$	$2n1p$	> 15(1)
	[3 $\leq$ $E$ $\leq$ 60]	—	—	(exclusive)	2.68			
$t$	8.6(6)(3)	9.80(22)(41)	—	—	—			
	[5 $\leq$ $E$ $\leq$ 17]	—	—	—	—			
$Z = 1$ sum	2.72(33)(10)	—	—	—	—	$^A\text{Mg}$	$xn1p$	> 128(8)
	[4 $\leq$ $E$ $\leq$ 60]	—	—	—	—			
$^3\text{He}$	1.49(24)(5)	1.70(8)(10)	—	—	—	$^{25}\text{Na}$	$1n2p$	2.4(17)
	[6 $\leq$ $E$ $\leq$ 17]	—	—	—	—			
$\alpha$	—	—	—	—	—	$^{24}\text{Na}$	$2n2p$	17.1(13)
$(\alpha + n)$	—	—	—	—	—	$^{23}\text{Na}$	$3n2p$	> 5(5)
	$^6\text{He}$	> 0.03	—	—	—			
$Z = 2$ sum	> 25.6(18)(10)	—	—	—	29.1	$^A\text{Na}$	$xn2p$	> 26(5)
$Z > 2$	> 0.013	—	—	—	—	$^{20}\text{F}$	$4n4p$	1.16(21)
charged particle total	> 141(3)(5)	171(30)	150(20)	144	—	$xnyp$		
		[1.4 $\leq$ $E$ $\leq$ 26]	—	—	—	$(y > 0)$		

crepancy originates primarily from an overestimation of the low-energy evaporation component in the calculation.

In contrast, the calculated yields for deuterons and tritons show good agreement with the experimental data within uncertainties. The  $\alpha$ -particle yield is also reproduced reasonably well by the MEM calculation, indicating that the model provides a satisfactory description of composite-particle emission channels.

The selective overestimation observed only for protons may be related to the competition with neutron emission in the calculation, particularly in the low-energy region. Since neutron emission is not directly constrained by the present experiment, further clarification will require dedicated measurements of neutron energy spectra extending down to low energies.

In this context, it is worth noting that, in the original MEM literature [35], the calculated neutron spectra were compared with the experimental data by Sundelin [56] and Kozlowski [57], and were found to slightly underestimate the measured yields in the low-energy region. Moreover, the available neutron data in those measurements have a lower energy limit of 4.25 MeV and therefore do not provide constraints on the low-energy region extending to energies as low as those accessible for protons, where the neutron yield is expected to increase sig-

nificantly. The lack of experimental information in this energy range may thus contribute to the uncertainty in the balance between proton and neutron emission in the model calculations.

### 3. Comparison to branching ratio measurement

Branching-ratio measurements of residual nuclei provide complementary insight into the competition between composite-particle emission and multiple-particle emission following  $\mu$ NC. In this subsection, the charged-particle yields obtained in the present work are compared with the branching-ratio measurement reported in Ref. [6]. A quantitative comparison of the integrated charged-particle yields obtained in the present work with the branching ratios deduced from activation measurements, together with the lower limits obtained using prompt  $\gamma$ -ray measurements, is summarized in Table V. The branching ratios quoted here correspond to  $\mu$ NC in  $^{28}\text{Si}$ , rather than in  $^{nat}\text{Si}$ , in order to ensure an unambiguous correspondence between charged-particle emission channels and residual nuclei. Given that  $^{28}\text{Si}$  has a natural abundance of approximately 92%, this choice is considered adequate for the present comparison.

First, the integrated yield of the proton emission spectrum is significantly larger than the branching ratio for the  $0n1p$  channel, whereas the integrated yield of the deuteron emission spectrum is substantially smaller than the branching ratio for the  $1n1p$  channel. This indicates that proton emission is mostly accompanied by the emission of one or more neutrons. Such behavior suggests that, in the de-excitation following  $\mu$ NC, the emission of protons and neutrons as separate particles is favored over the emission of bound deuterons. Consistently, the summed branching ratios of the  $xn1p$  channels are found to be in overall agreement with the sum of the integrated proton, deuteron, and triton yields, noting that both quantities represent lower limits.

A similar behavior, though less pronounced, is observed for  $\alpha$ -particle emission. The integrated yield of the  $\alpha$ -emission spectrum is significantly larger than the branching ratio for the  $2n2p$  channel, while the lower limit of the branching ratio for the  $3n2p$  channel amounts to a substantial fraction of that for the  $2n2p$  channel. This suggests that  $\alpha$  emission is also likely to be accompanied by neutron emission.

To elucidate how such multiple particles are emitted and whether they exhibit correlations, coincidence measurements are necessary. Nevertheless, charged-particle energy spectra and residual-nucleus branching-ratio measurements provide complementary information. Their combined use offers important constraints for refining theoretical descriptions of  $\mu$ NC.

### C. Observation of rare charged-particle emission channels

In addition to protons, deuterons, tritons, and  $\alpha$  particles, a very small number of events attributable to rarer charged-particle emission channels were observed in the present experiment. In the 200- $\mu$ m target run, events consistent with the emission of  $^3\text{He}$  or  $^6\text{He}$  were identified based on DPSA. Owing to the extremely limited statistics and the substantial energy loss in the thick target, it was not possible to reconstruct their initial energy spectra.

Furthermore, a few number of events corresponding to particles with  $Z > 2$  were also observed. These events may be associated with the emission of heavier clusters, such as  $^8\text{Be}$ , although the present data do not allow a definitive identification or a quantitative characterization of these channels.

To our knowledge, emissions of  $^3\text{He}$ ,  $^6\text{He}$ , and particles with  $Z > 2$  following  $\mu$ NC have not been reported in previous experimental studies. The present observation therefore extends the range of charged particles identified after  $\mu$ NC, albeit at a purely qualitative level.

At present, it remains unclear whether these rare channels originate from evaporation-like processes, preequilibrium mechanisms, or other reaction pathways activated at high excitation energies. In this context, it is worth

noting that a non-negligible contribution from  $4n4p$  decay branches following  $\mu$ NC at  $^{28}\text{Si}$ , corresponding in terms of particle composition to  $2\alpha$  emission, has been reported in the branching-ratio measurement [6]. Such observations suggest that multi-nucleon emission channels involving strong correlations among constituent nucleons may play a significant role in the decay process.

A detailed investigation of the production mechanisms of rare charged particles, including possible connections to correlated multi-nucleon emission, would require dedicated measurements with improved statistics and optimized sensitivity to heavy-cluster emission, which are beyond the scope of the present work.

## VI. CONCLUSIONS

In this work, we measured the energy spectra of charged particles emitted following  $\mu$ NC in silicon at the RIKEN-RAL muon facility. Compared with existing measurements, a more comprehensive set of spectral data was obtained over a wide energy range. In particular, the present experiment provides, for the first time, experimental information on the low-energy  $\alpha$ -particle spectrum, which had not been available in previous studies.

The measured spectra were compared with calculations based on the MEM and the PHITS code. For protons, both models reproduce the experimental spectra reasonably well.

For  $\alpha$  particles, however, the comparison reveals a clear model-dependent behavior. In the MEM calculation, the low-energy part of the spectrum, which is dominated by the evaporation component, is reproduced well, whereas the high-energy component attributed to preequilibrium emission is significantly overestimated. In contrast, the PHITS calculations tend to overestimate the evaporation-dominated low-energy yield, while providing a comparatively better description of the preequilibrium-driven high-energy component.

For deuterons and tritons, the MEM calculation reproduces the spectral shapes well over a wide energy range, while the PHITS calculations significantly underestimate the yields even after incorporating the effects of meson-exchange currents and the surface coalescence model.

These comparisons indicate that, even among composite particles, the balance between evaporation and preequilibrium emission is described differently by the two models, and that intrinsic differences exist in the emission mechanisms of  $d$ ,  $t$  and  $\alpha$  particles following  $\mu$ NC.

The present data provide valuable constraints for theoretical model descriptions of charged-particle emission after  $\mu$ NC. Systematic measurements of charged-particle energy spectra for other target nuclei will further contribute to improving models of preequilibrium and evaporation processes in  $\mu$ NC reactions.

While the present work is based on single-particle measurements, the results presented here clearly indicate that

future coincidence measurements of charged particles, in particular in combination with neutron detection, will be essential for a more complete understanding of multi-particle emission processes following  $\mu$ NC.

## ACKNOWLEDGMENTS

The authors would like to thank the accelerator staff at RAL for providing high-quality beam. The experiment was conducted under Program No. 2070004 at the ISIS Neutron and Muon Source at RAL. This work was partially supported by JSPS KAKENHI Grant Numbers JP19H05664 and JP21H01863.

## Appendix A: Fitting Function for Peak Timing Distribution

The peak timing distribution shown in Sect. III A was fitted using a composite function that accounts for two identical beam bunches separated by a fixed time interval  $\Delta t$ . The total fitting function is defined as

$$f(t) = f_1(t) + f_1(t - \Delta t), \quad (\text{A1})$$

where  $f_1(t)$  represents the contribution from a single beam bunch and is defined by

$$f_1(t) = A_e \mathcal{N}(t; \mu_e, \sigma_e) + A_\mu \mathcal{N}(t; \mu_\mu, \sigma_\mu) + A_{\text{decay}} \mathcal{D}(t; \mu_\mu, \sigma_\mu, \tau). \quad (\text{A2})$$

The first term represents prompt signals from electrons produced simultaneously with the muon beam, the second term corresponds to prompt signals from muons that are stopped in the plastic scintillator, and the third term describes delayed signals originating from decay electrons emitted by stopped muons, modeled as the convolution of an exponential decay with a Gaussian resolution function.

Here,  $\mathcal{N}(t; \mu, \sigma)$  denotes a Gaussian distribution:

$$\mathcal{N}(t; \mu, \sigma) = \frac{1}{\sqrt{2\pi}\sigma} \exp\left(-\frac{(t - \mu)^2}{2\sigma^2}\right), \quad (\text{A3})$$

and  $\mathcal{D}(t; \mu, \sigma, \tau)$  is the convolution of a Gaussian with an exponential decay characterized by a decay time constant  $\tau$ :

$$\mathcal{D}(t; \mu, \sigma, \tau) = \int_{-\infty}^t \mathcal{N}(t'; \mu, \sigma) e^{-(t-t')/\tau} dt' \quad (\text{A4})$$

$$= \frac{1}{2} \exp\left(-\frac{t - \mu}{\tau} + \frac{\sigma^2}{2\tau^2}\right) \times \text{erfc}\left(\frac{\mu - t + \sigma^2/\tau}{\sqrt{2}\sigma}\right). \quad (\text{A5})$$

The parameters  $A_\mu$ ,  $A_e$ , and  $A_{\text{decay}}$  denote the amplitudes of the muon, electron, and decay components, respectively. The parameter  $\tau$  is the decay time constant of the exponential, and  $\Delta t$  is the time interval between the two beam bunches.

In total, the fitting function includes nine free parameters:  $A_e$ ,  $\mu_e$ ,  $\sigma_e$ ,  $A_\mu$ ,  $\mu_\mu$ ,  $\sigma_\mu$ ,  $A_{\text{decay}}$ ,  $\tau$ , and  $\Delta t$ .

---

[1] D. Measday, The nuclear physics of muon capture, *Physics Reports* **354**, 243 (2001).

[2] W. U. Schröder, U. Jahnke, K. H. Lindenberger, G. Röschert, R. Engfer, and H. K. Walter, Spectra of neutrons from  $\mu$  capture in thallium, lead and bismuth, *Zeitschrift für Physik* **268**, 57 (1974).

[3] A. Wyttenbach, P. Baertschi, S. Bajo, J. Hadermann, K. Junker, S. Katcoff, E. A. Hermes, and H. S. Pruys, Probabilities of muon induced nuclear reactions involving charged particle emission, *Nuclear Physics A* **294**, 278 (1978).

[4] M. Niikura, T. Y. Saito, T. Matsuzaki, K. Ishida, and A. Hillier, Measurement of the production branching ratios following nuclear muon capture for palladium isotopes using the in-beam activation method, *Physical Review C* **109**, 014328 (2024).

[5] Y. Yamaguchi, M. Niikura, R. Mizuno, M. Tampo, M. Harada, N. Kawamura, I. Umegaki, S. Takeshita, and K. Haga, Measurement of radionuclide production probabilities in negative muon nuclear capture and validation of Monte Carlo simulation model, *Nuclear Instruments and Methods in Physics Research Section B: Beam Interactions with Materials and Atoms* **567**, 165801 (2025).

[6] R. Mizuno, M. Niikura, T. Y. Saito, T. Matsuzaki, S. Abe, H. Fukuda, M. Hashimoto, A. D. Hillier, K. Ishida, N. Kawamura, S. Kawase, T. Kawata, K. Kitafuji, F. Minato, M. Oishi, A. Sato, K. Shimomura, P. Strasser, S. Takeshita, D. Tomono, and Y. Watanabe, Measurement of production branching ratio after muon nuclear capture reaction of Al and Si isotopes, *Physical Review C* **112**, 054305 (2025).

[7] G. Backenstoss, S. Charalambus, H. Daniel, W. Hamilton, U. Lynen, Ch. Von Der Malsburg, G. Poelz, and H. Povel, Nuclear  $\gamma$ -rays following muon capture, *Nuclear Physics A* **162**, 541 (1971).

[8] B. L. Johnson, T. P. Gorrige, D. S. Armstrong, J. Bauer, M. D. Hasinoff, M. A. Kovash, D. F. Measday, B. A. Moftah, R. Porter, and D. H. Wright, Observables in muon capture on  $^{23}\text{Na}$  and the effective weak couplings  $\tilde{g}_a$  and  $\tilde{g}_p$ , *Physical Review C* **54**, 2714 (1996).

[9] T. P. Gorrige, D. S. Armstrong, S. Arole, M. Boleman, E. Gete, V. Kuzmin, B. A. Moftah, R. Sedlar, T. J. Stocki, and T. Teterova, Measurement of partial muon capture rates in  $1s$ - $0d$  shell nuclei, *Physical Review C* **60**, 055501 (1999).

[10] T. Stocki, D. Measday, E. Gete, M. Saliba, B. Moftah, and T. Gorrige, Gamma rays from muon capture in  $^{14}\text{N}$ , *Nuclear Physics A* **697**, 55 (2002).

[11] D. F. Measday and T. J. Stocki,  $\gamma$  rays from muon capture in natural Ca, Fe, and Ni, *Physical Review C* **73**,

045501 (2006).

[12] D. F. Measday, T. J. Stocki, and H. Tam,  $\gamma$  rays from muon capture in I, Au, and Bi, *Physical Review C* **75**, 045501 (2007).

[13] D. F. Measday, T. J. Stocki, B. A. Moftah, and H. Tam,  $\gamma$  rays from muon capture in  $^{27}\text{Al}$  and natural Si, *Physical Review C - Nuclear Physics* **76**, 1 (2007).

[14] D. Zinatulina, V. Brudanin, V. Egorov, C. Petitjean, M. Shirchenko, J. Suhonen, and I. Yutlandov, Ordinary muon capture studies for the matrix elements in  $\beta\beta$  decay, *Physical Review C* **99**, 024327 (2019).

[15] G. Heusser and T. Kirsten, Radioisotope production rates by muon capture, *Nuclear Physics A* **195**, 369 (1972).

[16] B. Heisinger, D. Lal, A. J. T. Jull, P. Kubik, S. Ivy-Ochs, K. Knie, and E. Nolte, Production of selected cosmogenic radionuclides by muons: 2. Capture of negative muons, *Earth and Planetary Science Letters* **200**, 357 (2002).

[17] S. E. Sobottka and E. L. Wills, Energy Spectrum of Charged Particles Emitted Following Muon Capture in  $\text{Si}^{28}$ , *Physical Review Letters* **20**, 596 (1968).

[18] Y. G. Budyashov, A. D. Zinov, A. D. Konin, A. I. Mukhin, and A. M. Chatrchyan, Charged particles from the capture of negative muons by the nuclei  $^{28}\text{Si}$ ,  $^{32}\text{S}$ ,  $^{40}\text{Ca}$ , and  $^{64}\text{Cu}$ , *Journal of Experimental and Theoretical Physics* (1971).

[19] A. Edmonds, J. Quirk, M. L. Wong, D. Alexander, R. H. Bernstein, A. Daniel, E. Diociaiuti, R. Donghia, E. L. Gillies, E. V. Hungerford, P. Kammel, B. E. Krikler, Y. Kuno, M. Lancaster, R. P. Litchfield, J. P. Miller, A. Palladino, J. Repond, A. Sato, I. Sarra, S. R. Soleti, V. Tishchenko, N. H. Tran, Y. Uchida, P. Winter, and C. Wu, Measurement of proton, deuteron, triton, and  $\alpha$  particle emission after nuclear muon capture on Al, Si, and Ti with the AlCap experiment, *Physical Review C* **105**, 1 (2022), 2110.10228.

[20] S. Manabe, Y. Watanabe, M. Niikura, K. Nakano, K. Nakano, T. Y. Saito, D. Suzuki, Y. Kawashima, D. Tomono, A. Sato, and H. Harano, Emissions of Hydrogen Isotopes from the Nuclear Muon Capture Reaction in  $^{nat}\text{Si}$ , *EPJ Web of Conferences* **284**, 01029 (2023).

[21] S. Manabe, Y. Watanabe, W. Liao, M. Hashimoto, K. Nakano, H. Sato, T. Kin, S. I. Abe, K. Hamada, M. Tampo, and Y. Miyake, Negative and Positive Muon-Induced Single Event Upsets in 65-nm UTBB SOI SRAMs, *IEEE Transactions on Nuclear Science* **65**, 1742 (2018).

[22] W. Liao, M. Hashimoto, S. Manabe, Y. Watanabe, S. I. Abe, K. Nakano, H. Takeshita, M. Tampo, S. Takeshita, and Y. Miyake, Negative and Positive Muon-Induced SEU Cross Sections in 28-nm and 65-nm Planar Bulk CMOS SRAMs, *IEEE International Reliability Physics Symposium Proceedings 2019-March*, 1 (2019).

[23] J.-L. Autran and D. Munteanu, Interactions of Low-Energy Muons with Silicon: Numerical Simulation of Negative Muon Capture and Prospects for Soft Errors, *Journal of Nuclear Engineering* **5**, 91 (2024).

[24] T. Matsuzaki, K. Ishida, K. Nagamine, I. Watanabe, G. Eaton, and W. Williams, The RIKEN-RAL pulsed Muon Facility, *Nuclear Instruments and Methods in Physics Research Section A: Accelerators, Spectrometers, Detectors and Associated Equipment* **465**, 365 (2001).

[25] A. D. Hillier, J. S. Lord, K. Ishida, and C. Rogers, Muons at ISIS, *Philosophical Transactions of the Royal Society A: Mathematical, Physical and Engineering Sciences* **377**, 20180064 (2018).

[26] S. Kawase, T. Murota, H. Fukuda, M. Oishi, T. Kawata, K. Kitafuji, S. Manabe, Y. Watanabe, H. Nishibata, S. Go, T. Kai, Y. Nagata, T. Muto, Y. Ishibashi, M. Niikura, D. Suzuki, T. Matsuzaki, K. Ishida, R. Mizuno, and N. Kitamura, Effect of large-angle incidence on particle identification performance for light-charged ( $Z \leq 2$ ) particles by pulse shape analysis with a pad-type nTD silicon detector, *Nuclear Instruments and Methods in Physics Research Section A: Accelerators, Spectrometers, Detectors and Associated Equipment* **1059**, 168984 (2024).

[27] CAEN S.p.A., *CoMPASS User Manual Rev. 25* (2025).

[28] T. Suzuki, D. F. Measday, and J. P. Roalsvig, Total nuclear capture rates for negative muons, *Physical Review C* **35**, 2212 (1987).

[29] S. Agostinelli, J. Allison, K. Amako, J. Apostolakis, H. Araujo, P. Arce, M. Asai, D. Axen, S. Banerjee, G. Barrand, F. Behner, L. Bellagamba, J. Boudreau, L. Broglia, A. Brunengo, H. Burkhardt, S. Chauvie, J. Chuma, R. Chytracek, G. Cooperman, G. Cosmo, P. Degtyarenko, A. Dell'Acqua, G. Depaola, D. Dietrich, R. Enami, A. Feliciello, C. Ferguson, H. Fesefeldt, G. Folger, F. Foppiano, A. Forti, S. Garelli, S. Giani, R. Giannitrapani, D. Gibin, J. Gómez Cadenas, I. González, G. Gracia Abril, G. Greeniaus, W. Greiner, V. Grichine, A. Grossheim, S. Guatelli, P. Gumpelinger, R. Hamatsu, K. Hashimoto, H. Hasui, A. Heikkinen, A. Howard, V. Ivanchenko, A. Johnson, F. Jones, J. Kallenbach, N. Kanaya, M. Kawabata, Y. Kawabata, M. Kawaguti, S. Kelner, P. Kent, A. Kimura, T. Kodama, R. Kokoulin, M. Kossov, H. Kurashige, E. Lamanna, T. Lampén, V. Lara, V. Lefebure, F. Lei, M. Liendl, W. Lockman, F. Longo, S. Magni, M. Maire, E. Medernach, K. Minamimoto, P. Mora De Freitas, Y. Morita, K. Murakami, M. Nagamatu, R. Nartallo, P. Nieminen, T. Nishimura, K. Ohtsubo, M. Okamura, S. O'Neale, Y. Oohata, K. Paech, J. Perl, A. Pfeiffer, M. Pia, F. Ranjard, A. Rybin, S. Sadilov, E. Di Salvo, G. Santin, T. Sasaki, N. Savvas, Y. Sawada, S. Scherer, S. Sei, V. Sirotenko, D. Smith, N. Starkov, H. Stoecker, J. Sulkimo, M. Takahata, S. Tanaka, E. Tcherniaev, E. Safai Tehrani, M. Tropeano, P. Truscott, H. Uno, L. Urban, P. Urban, M. Verderi, A. Walkden, W. Wander, H. Weber, J. Wellisch, T. Wenaus, D. Williams, D. Wright, T. Yamada, H. Yoshida, and D. Zschiesche, Geant4—a simulation toolkit, *Nuclear Instruments and Methods in Physics Research Section A: Accelerators, Spectrometers, Detectors and Associated Equipment* **506**, 250 (2003).

[30] J. Allison, K. Amako, J. Apostolakis, H. Araujo, P. Arce Dubois, M. Asai, G. Barrand, R. Capra, S. Chauvie, R. Chytracek, G. Cirrone, G. Cooperman, G. Cosmo, G. Cuttone, G. Daquino, M. Donszelmann, M. Dressel, G. Folger, F. Foppiano, J. Generowicz, V. Grichine, S. Guatelli, P. Gumpelinger, A. Heikkinen, I. Hrivnacova, A. Howard, S. Incerti, V. Ivanchenko, T. Johnson, F. Jones, T. Koi, R. Kokoulin, M. Kossov, H. Kurashige, V. Lara, S. Larsson, F. Lei, O. Link, F. Longo, M. Maire, A. Mantero, B. Mascialino, I. McLaren, P. Mendez Lorenzo, K. Minamimoto, K. Murakami, P. Nieminen, L. Pandola, S. Parlati, L. Peralta, J. Perl, A. Pfeiffer, M. Pia, A. Ribon, P. Rodrigues, G. Russo, S. Sadilov, G. Santin, T. Sasaki, D. Smith, N. Starkov,

S. Tanaka, E. Tcherniaev, B. Tome, A. Trindade, P. Truscott, L. Urban, M. Verderi, A. Walkden, J. Wellisch, D. Williams, D. Wright, and H. Yoshida, Geant4 developments and applications, *IEEE Transactions on Nuclear Science* **53**, 270 (2006).

[31] J. Allison, K. Amako, J. Apostolakis, P. Arce, M. Asai, T. Aso, E. Bagli, A. Bagulya, S. Banerjee, G. Barraud, B. Beck, A. Bogdanov, D. Brandt, J. Brown, H. Burkhardt, Ph. Canal, D. Cano-Ott, S. Chauvie, K. Cho, G. Cirrone, G. Cooperman, M. Cortés-Giraldo, G. Cosmo, G. Cuttone, G. Depaola, L. Desorgher, X. Dong, A. Dotti, V. Elvira, G. Folger, Z. Francis, A. Galoyan, L. Garnier, M. Gayer, K. Genser, V. Grichine, S. Guatelli, P. Guéye, P. Gumplinger, A. Howard, I. Hřivnáčová, S. Hwang, S. Incerti, A. Ivanchenko, V. Ivanchenko, F. Jones, S. Jun, P. Kaitaniemi, N. Karakatsanis, M. Karamitros, M. Kelsey, A. Kimura, T. Koi, H. Kurashige, A. Lechner, S. Lee, F. Longo, M. Maire, D. Mancusi, A. Mantero, E. Mendoza, B. Morgan, K. Murakami, T. Nikitina, L. Pandola, P. Paprocki, J. Perl, I. Petrović, M. Pia, W. Pokorski, J. Quesada, M. Raine, M. Reis, A. Ribon, A. Ristić Fira, F. Romano, G. Russo, G. Santin, T. Sasaki, D. Sawkey, J. Shin, I. Strakovský, A. Taborda, S. Tanaka, B. Tomé, T. Toshito, H. Tran, P. Truscott, L. Urban, V. Uzhinsky, J. Verbeke, M. Verderi, B. Wendt, H. Wenzel, D. Wright, D. Wright, T. Yamashita, J. Yarba, and H. Yoshida, Recent developments in Geant4, *Nuclear Instruments and Methods in Physics Research Section A: Accelerators, Spectrometers, Detectors and Associated Equipment* **835**, 186 (2016).

[32] T. J. Roberts and D. M. Kaplan, G4beamline simulation program for matter-dominated beamlines, in *2007 IEEE Particle Accelerator Conference (PAC)* (2007) pp. 3468–3470.

[33] L. Brenner, R. Balasubramanian, C. Burgard, W. Verkerke, G. Cowan, P. Verschuur, and V. Croft, Comparison of unfolding methods using RooFitUnfold, *International Journal of Modern Physics A* **35**, 2050145 (2020).

[34] G. D'Agostini, A multidimensional unfolding method based on Bayes' theorem, *Nuclear Instruments and Methods in Physics Research Section A: Accelerators, Spectrometers, Detectors and Associated Equipment* **362**, 487 (1995).

[35] F. Minato, T. Naito, and O. Iwamoto, Nuclear many-body effects on particle emission following muon capture on  $^{28}\text{Si}$  and  $^{40}\text{Ca}$ , *Physical Review C* **107**, 054314 (2023).

[36] T. Sato, Y. Iwamoto, S. Hashimoto, T. Ogawa, T. Furuta, S. Abe, T. Kai, Y. Matsuya, N. Matsuda, Y. Hirata, T. Sekikawa, L. Yao, P.-E. Tsai, H. N. Ratliff, H. Iwase, Y. Sakaki, K. Sugihara, N. Shigyo, L. Sihver, and K. Niita, Recent improvements of the particle and heavy ion transport code system – PHITS version 3.33, *Journal of Nuclear Science and Technology* **61**, 127 (2024).

[37] J. S. O'Connell, T. W. Donnelly, and J. D. Walecka, Semileptonic Weak Interactions with  $\text{C}^{12}$ , *Physical Review C* **6**, 719 (1972).

[38] F. Minato, Estimation of a 2p2h effect on Gamow-Teller transitions within the second Tamm-Dancoff approximation, *Physical Review C* **93**, 044319 (2016).

[39] P.-G. Reinhard, D. J. Dean, W. Nazarewicz, J. Dobaczewski, J. A. Maruhn, and M. R. Strayer, Shape coexistence and the effective nucleon-nucleon interaction, *Physical Review C* **60**, 014316 (1999).

[40] N. Van Giai and H. Sagawa, Spin-isospin and pairing properties of modified Skyrme interactions, *Physics Letters B* **106**, 379 (1981).

[41] M. Lifshitz and P. Singer, Meson-exchange currents and energetic particle emission from  $\mu^-$  capture, *Nuclear Physics A* **476**, 684 (1988).

[42] C. Kalbach, Two-component exciton model: Basic formalism away from shell closures, *Physical Review C* **33**, 818 (1986).

[43] A. Koning and M. Duijvestijn, A global pre-equilibrium analysis from 7 to 200 MeV based on the optical model potential, *Nuclear Physics A* **744**, 15 (2004).

[44] W. Hauser and H. Feshbach, The Inelastic Scattering of Neutrons, *Physical Review* **87**, 366 (1952).

[45] O. Iwamoto, N. Iwamoto, S. Kunieda, F. Minato, and K. Shibata, The CCONE Code System and its Application to Nuclear Data Evaluation for Fission and Other Reactions, *Nuclear Data Sheets* **131**, 259 (2016).

[46] S. Abe and T. Sato, Implementation of muon interaction models in PHITS, *Journal of Nuclear Science and Technology* **54**, 101 (2017).

[47] P. Singer, Neutron emission following muon capture in heavy nuclei, *Il Nuovo Cimento (1955-1965)* **23**, 669 (1962).

[48] K. Niita, S. Chiba, T. Maruyama, T. Maruyama, H. Takada, T. Fukahori, Y. Nakahara, and A. Iwamoto, Analysis of the  $(N, xN')$  reactions by quantum molecular dynamics plus statistical decay model, *Physical Review C* **52**, 2620 (1995).

[49] T. Ogawa, T. Sato, S. Hashimoto, D. Satoh, S. Tsuda, and K. Niita, Energy-dependent fragmentation cross sections of relativistic  $^{12}\text{C}$ , *Physical Review C* **92**, 024614 (2015).

[50] S. Furihata, Statistical analysis of light fragment production from medium energy proton-induced reactions, *Nuclear Instruments and Methods in Physics Research Section B: Beam Interactions with Materials and Atoms* **171**, 251 (2000).

[51] S. Furihata, The GEM Code - the Generalized Evaporation Model and the Fission Model, in *Advanced Monte Carlo for Radiation Physics, Particle Transport Simulation and Applications*, edited by A. Kling, F. J. C. Barão, M. Nakagawa, L. Távora, and P. Vaz (Springer Berlin Heidelberg, Berlin, Heidelberg, 2001) pp. 1045–1050.

[52] Y. Watanabe and D. N. Kadrev, Extension of quantum molecular dynamics for production of light complex particles in nucleon-induced reactions, in *ND2007* (EDP Sciences, Nice, France, 2007) pp. 1121–1124.

[53] A. Iwamoto and K. Harada, Mechanism of cluster emission in nucleon-induced preequilibrium reactions, *Physical Review C* **26**, 1821 (1982).

[54] K. Sato, A. Iwamoto, and K. Harada, Pre-equilibrium emission of light composite particles in the framework of the exciton model, *Physical Review C* **28**, 1527 (1983).

[55] M. Lifshitz and P. Singer, Nuclear excitation function and particle emission from complex nuclei following muon capture, *Physical Review C* **22**, 2135 (1980).

[56] R. M. Sundelin and R. M. Edelstein, Neutron Asymmetries and Energy Spectra from Muon Capture in Si, S, and Ca, *Physical Review C* **7**, 1037 (1973).

[57] T. Kozłowski, W. Bertl, H. P. Povel, U. Sennhauser, H. K. Walter, A. Zglinski, R. Engfer, CH. Grab, E. A. Hermes, H. P. Isaak, A. Van Der Schaaf, J. Van Der Pluym, and W. H. A. Hesselink, Energy spectra and

asymmetries of neutrons emitted after muon capture, Nuclear Physics A **436**, 717 (1985).